Experimental and theoretical analysis of TiO_2 powders flow properties at ambient and high temperatures

Domenico Macrì[a*], Diego Barletta[b], Paola Lettieri[a], Massimo Poletto[b]

[a] Department of Chemical Engineering, University College London, London WC1E 7JE, UK
[b] Dipartimento di Ingegneria Industriale, Università degli Studi di Salerno, Via Giovanni Paolo II, 132-I-84084 Fisciano (SA), Italy
*Corresponding author. Tel. +44 (0)20 76797868; E-mail address: domenico.macri.14@ucl.ac.uk

Highlights

- Temperature effect on bulk flow properties of TiO_2 powders is evaluated experimentally.
- Measured properties are related to the microscopic IPFs by theoretical models.
- A sensitivity analysis on models' parameters is performed.

1. Abstract

Changes of bulk flow properties of two different types of titanium dioxide powders are measured at room temperature and 500 °C using the High Temperature Annular Shear Cell. A significant increase of the macroscopic bulk flow properties is observed with increasing temperature, in particular with regards to the unconfined yield strength. Two different modelling approaches are proposed with the aim to relate the measured properties to the microscopic interactions between particles. The results indicate that both the model provides a good match with the experimental data when proper values for the models' parameters are taken into account. To this end, the sensitivity analysis for the main parameters of the models is performed.

Keywords: interparticle forces, powder flow properties, high temperature

2. Introduction

Bulk flow properties of particulate materials play a significant role in several industrial process units, such as fluidized beds, granulators and dryers. Powders flow behaviour is commonly described by using a continuum mechanics methodology, which allows to estimate the stress distribution within powders (Janssen, 1895; Walker, 1966; Walters, 1973). Such a practice is also used by engineers to design equipment for the storage and handling of particulate materials (Fitzpatrick et al., 2004; Chen et al., 2012).

The stress distribution inside a bulk solid is usually described combining Yield Locus and Mohr circles analysis. The Yield Locus analysis is aimed at determining the limiting shear

stresses under any normal stress when failure, or to be precise, flow occurs. It is designed to evaluate the angle of internal friction (ϕ_i) and the cohesion (C) for a sample material and then calculate its overall strength under compressive load. Assuming that the particles behaves like a solid in the failure conditions, the local state of stresses can be represented in the normal-shear stresses plane (σ-τ plane) by Mohr's circles tangent to the yield locus. They can be used to evaluate the major principle stress (σ_1) and the unconfined yield stress (fc) (Nedderman, 1992).

Many testers are available for powder flowability characterisation. However, for design purposes, the shear cells are currently the most used devices (Jenike, 1964; Schwedes, 2003; Lettieri and Macrì, 2016). These tests, first introduced by Jenike in 1953, are commonly distinguished between indirect and direct shear testers. The former are divided into uniaxial, biaxial and triaxial testers. The latter can be translational or rotational. Examples of translational direct testers are Jenike's and Casagrande's shear testers, while some of the most important rotational direct testers are the torsional and the ring shear testers, like the Schulze shear cell (Schulze, 1994a, 1994b, 2007).

The flowability of powders is strongly related to the type and magnitude of the microscopic interactions between particles. Furthermore, the flow properties at realistic process conditions need to be evaluated in order to analyse to what extent physical and mechanical particle properties (Pilpel and Britten, 1979; Fu et al., 2012; Liang et al., 2012), temperature (Kanaoka et al., 2001; Tomasetta et al., 2011; Chirone et al., 2016), humidity (Pierrat and Caram, 1997; Pierrat et al., 1998; Teunou and Fitzpatrick, 1999; Gröger et al., 2003; Landi et al., 2011) and loosely compacted conditions (Kono et al., 1994; Bruni et al., 2007b; Barletta and Poletto, 2012) affect the flow behaviour.

Some authors assessed the effects of interparticle interactions on the flow characteristics of particulate materials through direct measurements of the forces acting between particles (IPFs) (Quintanilla et al., 2001; Forsyth et al., 2002; Pagliai et al., 2006; Tanaka et al., 2008). IPFs are enhanced when the consolidation level is low, as in the case of aerated and fluidised beds where buoyancy force is balanced by the fluid drag force. During these processes, the powder flow behaviour is related to relative weight of the interparticle forces compared to the hydrodynamic forces (HDFs) (Mutsers and Rietema, 1977; Molerus, 1982; Rietema et al., 1993; Hou et al., 2012).

Several studies available in the literature have addressed the experimental evaluation of the effect of temperature on fluidization behaviour (Xie and Geldart, 1995; Formisani et al., 1998, 2002; Lettieri et al., 2000, 2002; Bruni et al., 2006), showing a significant change that

cannot be entirely explained by taking into account only hydrodynamic forces. The authors provided an interpretation based on the hypothesis that temperature could increase the relative weight of IPFs with respect to HDFs.

On one hand direct measurements of interparticle forces as a function of temperature result still difficult to perform and they are affected by a significant uncertainty (Pagliai et al., 2006). On the other hand, interparticle force variations with temperature can be correlated to the cohesion changes, measured with shear testers. Moreover, the measured flow properties can be linked to the fluidization behaviour of powders (Barletta, 2004; Bruni et al., 2007a; Johanson and Tomasetta et al., 2012). Powder cohesion can be related to the intensity of IPFs such as van der Waals, electrostatic and capillary forces, which are affected by temperature as a result of changes of particle hardness, liquid bridge formation or variations of the dielectric characteristics.

Few experimental works are available in literature on the influence of temperature on powders flow properties (Hurley et al., 2006; Zimmerlin et al., 2008; Ripp and Ripperger, 2010). Tomasetta et al. (2013, 2014) recently modified at the University of Salerno a Schulze shear cell to perform measurements up to 500 °C. They evaluated the yield loci at ambient temperature and at 500 °C for different samples: glass beads, FCC powder, fly ashes, alumina and natural corundum. The results showed that there was no significant effect of the temperature in the range 20–500 °C on the shear flow of the FCC powder, alumina, fly ashes and corundum powder. Instead, an increase of cohesion and, therefore, of the unconfined yield strength was observed with temperature for glass beads. More recently, Chirone et al. (2016) used the high-temperature annular shear cell developed by Tomasetta and co-workers to characterize the bulk flow properties of five ceramic powder samples with different particle size distributions between ambient temperature and 500 °C. Furthermore, they used the model based on the multiscale approach proposed by Rumpf (1970) and Molerus (1975, 1978) to predict the effect of temperature on the tensile strength of the powder samples. They observed a significant increase of powder cohesion at 500 °C for different cuts of the same powder with a particle size larger than 20 μm, resulting in a lower flowability of the samples.

Within this framework, this work presents experimental observations on the effect of temperature on the flow behaviour of various titanium ore powders. To this end, rheological measurements were performed using the modified Schulze shear cell to assess the particle-particle interactions at both ambient and high temperature.

In addition, two different modelling procedures are proposed in order to relate the microscopic interparticle interactions to the measured macroscopic bulk flow properties.

Modelling approaches based on Rumpf and Molerus theories (Rumpf, 1970; Molerus, 1975, 1978) and on Tomas' (Tomas, 2000, 2001a, 2001b, 2004) have been followed. An accurate analysis of both models has been carried out on the basis of a sensitivity analysis on the main models parameters.

3. Theoretical framework

In order to relate interparticle interactions to bulk flow properties, models based on both Tomas (2000, 2001a, 2001b, 2004) and Rumpf-Molerus theories (Rumpf, 1970; Molerus, 1975, 1978) for steady-state flow of fine and cohesive particulate solids can be used. Such theories are based on the assumption that consolidation and non-rapid flow of particulate solids can be related with adhesion forces in particles contacts, and they include the failure hypotheses of Tresca and Coulomb-Mohr and the yield locus concept of Jenike (Jenike et al., 1960; Jenike, 1962) as well as the Warren-Spring Equations (Ashton et al., 1965; Cheng, 1968; Stainforth et al., 1971; Stainforth and Ashley, 1973; Stainforth and Berry, 1973).

First of all, according to Tomas, it is important to consider what kind of mechanical deformation occurs when an external compressive normal force F_N is acting on particles that are very close to each other. There are four main different kind of mechanical interactions that can occur on the particle surface contacts, each characterised by a different physical behaviour, which in turn is influenced by particle material characteristics. These can be identified as follows:

1. Reversible elastic, in which deformation rate and consolidation do not bear time effects, these are generally valid for all particulate solids at least in a limited portion of the interparticle approach;
2. Irreversible plastic, in which deformation rate and consolidation are time invariant, these are typical for mineral powders;
3. Reversible viscoelastic, in which deformation rate and consolidation change with time, these are distinctive for cut post-consumer waste particles;
4. Irreversible viscoplastic, in which deformation rate and consolidation change with time variable, these apply to fine particle fusion.

Tomas (2000) reported a schematic diagram (Figure 1) of what happens when an external compressive normal force F_N is acting on isotropic, stiff, linear elastic and monodisperse spherical particles, highlighting how a contact point deforms to a contact area and how the adhesion force between the particles increases.

Both the microscale modelling approaches proposed in this work are based on the following main assumptions (Tomas, 2004; Tomasetta et al., 2014):

1. Particles are organised in a randomly packed assembly and the packing structure is assumed to be isotropic with uniform porosity (ε) in any cross-sectional area as well as in the powder bulk;
2. Particles are spherical and monodisperse and thus the contact points are uniformly distributed over the particle surface with equal probability;
3. The contact areas are small in comparison to the characteristic particle size, therefore these may be considered as contact points;
4. The transmission of an isostatic state of compressive stress with three equal principal stresses is assumed.

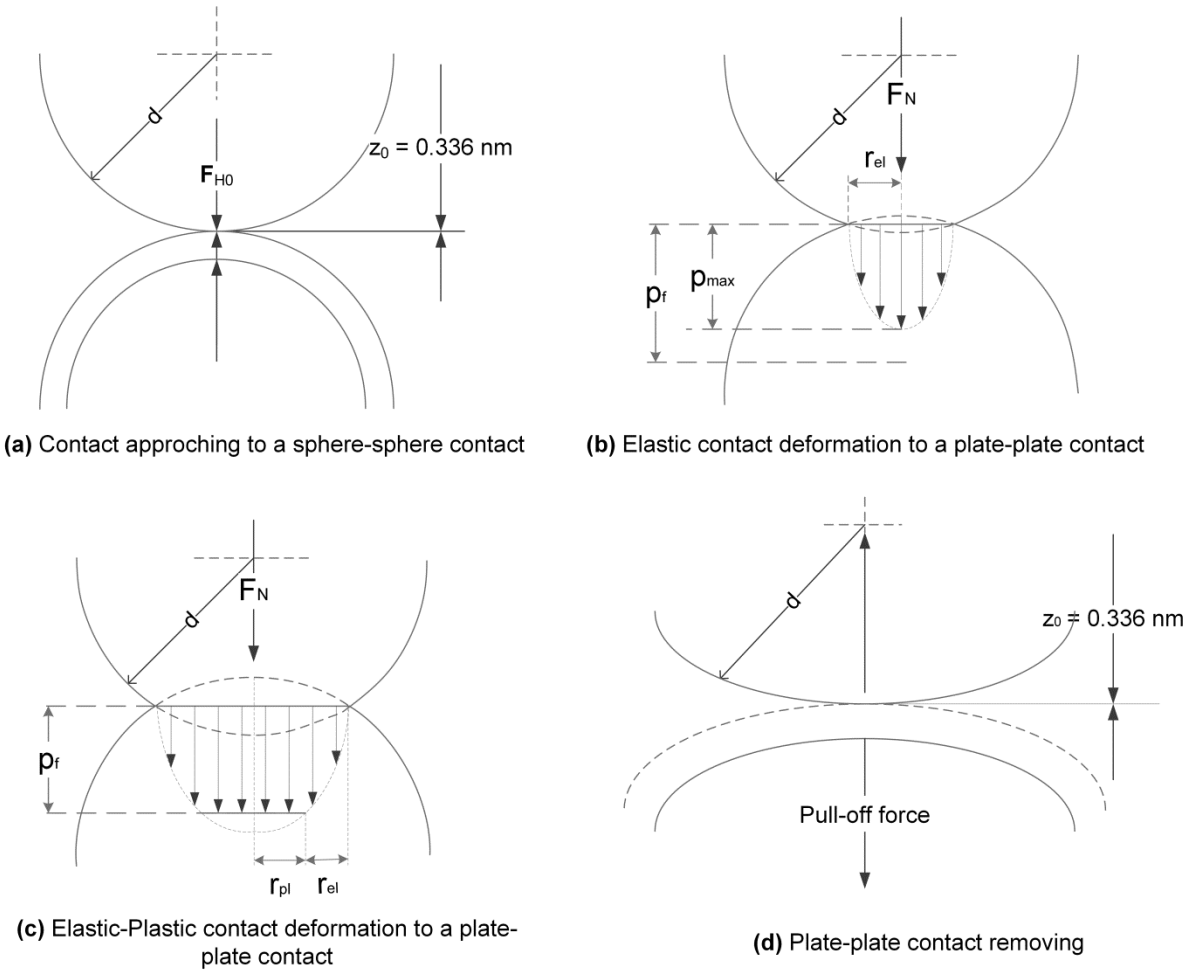

Figure 1 – Particle contact approaching, deformations and removing. Adapted from Tomas (2000).

These hypotheses are the basis of the equation derived by Molerus (1975) for the relationship between stresses and contact forces (F_c) for monodisperse particles with characteristic particle size d and assembly porosity ε:

$$\sigma = \frac{F_c}{d^2}\frac{1-\varepsilon}{\varepsilon} \quad \textbf{(1)}$$

Eqn. (1) can be used to relate the IPFs acting in a real bulk solid (F_H) to the isostatic tensile strength σ_t extrapolated from the powder experimental yield locus, i.e. the tensile stress at which the contact separation equals the adhesive interparticle forces F_H at the contact point:

$$F_H = \sigma_t \, d_{sv}^2 \frac{\varepsilon}{1-\varepsilon} \quad \textbf{(2)}$$

In which d_{sv} is the particle Sauter mean diameter, which should be used as the characteristic particle size for size distributed powders, because of it provides the best estimate of the ratio between particle surface and volume and it gives the most accurate volumetric concentration of the inter-particle contact points, which is the key variable to relate stresses to average interparticle forces values (Tomasetta et al., 2014).

Tomas stated that in order to properly describe the failure/flowability conditions of a bulk powder, an elastic-plastic particle contact model should be used. His theory is inspired by Rumpf-Molerus approach, but it also takes into account the theory proposed by Schubert et al. (1976) to combine the elastic and plastic contact strains using the annular elastic A_{el} and the circular plastic A_{pl} contact area, as well as the mathematical model developed by Thornton and Ning (1998) for the stick/bounce behaviour of adhesive and elastic-plastic particles.

$$F_H = F_{H0} + \frac{p_{VdW}}{p_f\left(1+\frac{2}{3}\frac{A_{el}}{A_{pl}}\right)} F_N \quad \textbf{(3)}$$

In which F_N is the compressive normal force transmitted at the contact during the consolidation stage, F_{H0} is the adhesion force without any consolidation (F_N =0) and any contact deformation intrinsically present in fine powders and related to their cohesive nature, p_{VdW} is the van der Waals pressure for a plate-plate model and p_f is the repulsive particle micro-hardness, i.e. the resistance against plastic deformation expressed as the plastic compressive yield strength of the particle material.

Tomas developed a normal force-displacement model starting from the particle contact force equilibrium between attraction and elastic/plastic repulsion. The diagram in Figure 2 describes a typical force-displacement diagram for elastic-plastic contact deformation, as reported by Tomas (2003). The compressive normal force F_N and the pull-off force acting

during the unloading stage are both taken into account. In particular, three different stages are shown: loading, unloading and reloading phase.

The loading stage is identified by the D-U segment in the diagram. The origin of this diagram ($h_c = 0$) is equivalent to the characteristic molecular separation distance between touching and non-continuous solids z_0. When the particles are approaching from an infinite distance $-\infty$ to this minimum separation distance z_0 the sphere–sphere contact without any contact deformation is formed by the attractive adhesion force F_{H0} intrinsically present in fine powders and related to their cohesive nature (point D in the diagram). Then the contact may be loaded from D to Y and, as a response, is elastically deformed with an approximate circular contact area according the curve labelled with Hertz (Figure 1b). When the maximum pressure in the contact centre reaches the micro-yield strength p_f at the yield point Y, the contact starts with plastic yielding (Y-U). The overall displacement h_c is expressed by the annular elastic A_{el} (thickness r_{el}) and the circular plastic A_{pl} (radius r_{pl}) contact area (Figure 1c).

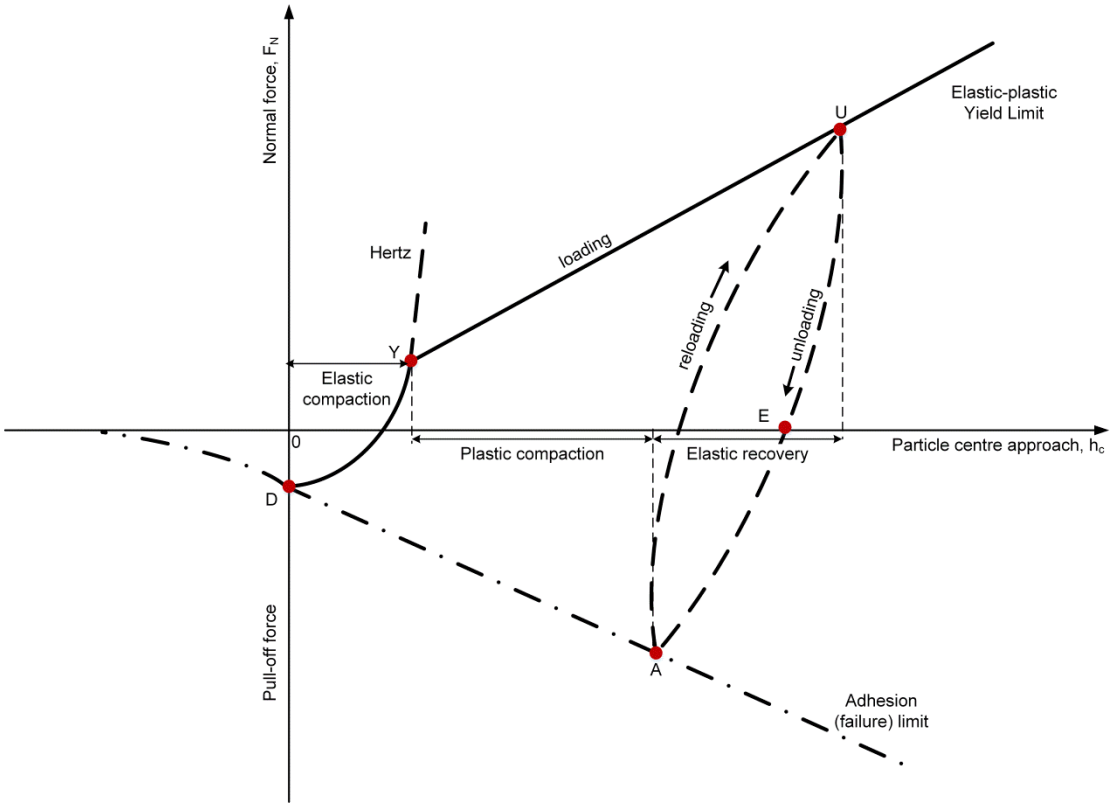

Figure 2 – Typical force-displacement diagram for elastic-plastic contact deformation of titania particles, Adopted from Tomas (2000).

As soon as a pull-off force is applied at an arbitrary point U, the unloading phase (U-E-A) begins. At first, the contact recovers elastically along an extended Hertzian parabolic curve (U-E) down to the perfect plastic displacement $h_{c,E}$. Then, beyond point E, the same curve

runs down to the intersection with the adhesion limit (point A). Thus, the elastically deformed annular contact zone is completely recovered and a plate-plate contact (Figure 1d) remains with a "frozen" radius $r_{c,A}$ and a reduced plastic displacement $h_{c,A}$. At this the point the contact between flattened particles fails and detaches with the increased distance $z = z_0 + h_{c,A} - h_c$. If a compressive normal force F_N is replaced, the reloading curve runs from point A to U symmetrically to curve U-A and the displacement $h_{c,U}$ is reached.

Within this framework, the author proposed a linear force-displacement model for particles with overall displacement h_c (Tomas, 2000, 2004).

$$F_{H0} + F_N = \frac{\pi}{4}\, d\, p_f \left(\kappa_A - \kappa_p\right) h_c \qquad \textbf{(4)}$$

Where κ_p is the plastic repulsion coefficient and κ_A is the elastic-plastic contact area coefficient representing the ratio of plastic particle deformation area A_{pl} to the total contact deformation area, which includes the contact area affected by elastic displacement $A_c = A_{pl} + A_{el}$. They can be estimated as:

$$\kappa_p = \frac{C_{H,sls}}{6\pi\, p_f\, z_0^3} \qquad \textbf{(5)}$$

$$\kappa_A = \frac{2}{3} + \frac{1}{3}\,\frac{A_{pl}}{A_c} = 1 - \frac{1}{3}\,\sqrt[3]{\frac{h_{c,f}}{h_c}} \qquad \textbf{(6)}$$

In which $h_{c,f}$ is the displacement for incipient yielding at $p = p_f$ that can be defined as function of particle size and the Hertz modulus of elasticity E^* (ν Poisson ratio and E Young's modulus):

$$h_{c,f} = d\,\left(\frac{\pi\, p_f}{2\, E^*}\right)^2 \qquad \textbf{(7)}$$

$$E^* = \frac{E}{1-\nu^2} \qquad \textbf{(8)}$$

Starting from Eqn. (4), Tomas obtained a general non-linear adhesion force model, in which the interparticle adhesive force F_H depend on the normal force applied F_N, the adhesion force F_{H0} without any consolidation and contact flattening, the extent of elastic-plastic deformation that is taken into account by an elastic-plastic consolidation coefficient κ, the radius of surface curvature r_c and the modulus of elasticity E^*.

However, he proposed a linearized form for the adhesion force model, that can be interpreted as a general linear particle contact constitutive model or, indeed, linear in forces and non-linear concerning material characteristics (see appendix A for calculation and superposition details):

$$F_H = \frac{\kappa_A}{\kappa_A - \kappa_p} F_{H0} + \frac{\kappa_p}{\kappa_A - \kappa_p} F_N = (1 + \kappa)\, F_{H0} + \kappa\, F_N \quad \textbf{(9)}$$

The elastic-plastic consolidation coefficient κ describes the influence of plastic contact deformation and so it is a measure of irreversible particle contact stiffness or softness. As shown in Eqn. (9), it can be defined as:

$$\kappa = \frac{\kappa_p}{\kappa_A - \kappa_p} \quad \textbf{(10)}$$

It is therefore given by the slope of the linear relationship between the interparticle adhesive force F_H and the normal force F_N: a small slope ($F_H \approx F_{H0}$) stands for low adhesion level because of stiff particle contacts, while a large inclination means soft contacts and a resulting cohesive flow behaviour.

The normal stress at consolidation σ_N was used to estimate the normal contact force F_N with Eqn. (1), assuming a uniform distribution of powder consolidation at contact points:

$$F_N = \sigma_N\, d_{sv}^2 \frac{\varepsilon}{1 - \varepsilon} \quad \textbf{(11)}$$

This assumption could be criticised by arguing that the Rumpf equation was derived in the hypothesis of an isostatic state of stress, in which there is a uniform distribution of contact forces on each particles. According to Molerus (1975) Eqn. (11) can be applied to any uniaxial state of stress and therefore to any state of stress. This may not necessarily true in general, but it appears reasonable in case limited tangential forces are applied on the plane on which the stress calculated by Eqn. (11) is estimated.

If a perfect plastic and irreversible contact displacement is considered ($A_{el} \to 0$) Eqn. (3) can be rewritten as:

$$F_H = F_{H0} + \frac{p_{VdW}}{p_f} F_N \quad \textbf{(12)}$$

That is the expression proposed by Rumpf-Molerus (Molerus, 1978, 1975; Rumpf, 1970) for the adhesion forces in presence of an external normal force F_N flattens the particle contact to a plate-plate contact:

$$F_H = F_0 + \kappa_{pl}\, F_N \quad \textbf{(13)}$$

In which F_N is the external normal force, F_0 is the adhesion force without any consolidation (F_N =0) and κ_{pl} is the plastic repulsion coefficient, that can be estimated according to Eqn. (14).

$$\kappa_{pl} = \frac{p_{VdW}}{p_f} \approx \frac{C_{H,sls}}{6\pi\, p_f\, z_0^3 \left(1 - \frac{C_{H,sls}}{6\pi\, p_f\, z_0^3}\right)} \quad \textbf{(14)}$$

Where $C_{H,sfs}$ is the Hamaker solid-fluid-solid constant and z_0 is the characteristic molecular separation distance, that amounts to about 0.3-0.4 nm (Krupp, 1967).

Moreover, Molerus (1978) proposed the following expression for the definition for F_0:

$$F_0 = \frac{C_{H,sls}\, r_{pl}}{12\, z_0^2 \left(1 - \frac{C_{H,sls}}{6\pi\, p_f\, z_0^3}\right)} \tag{15}$$

In which r_{pl} is the mean curvature radius at the contact point (which is not necessarily related to the particle size due to the probable surface local curvatures and asperities).

Thus, Eqn. (13) results in the following expression:

$$F_H = \frac{C_{H,sls}\, r_{pl}}{12\, z_0^2 \left(1 - \frac{C_{H,sls}}{6\pi\, p_f\, z_0^3}\right)} + \frac{C_{H,sls}}{6\pi\, p_f\, z_0^3 \left(1 - \frac{C_{H,sls}}{6\pi\, p_f\, z_0^3}\right)} F_N \tag{16}$$

The theories proposed by Molerus and Tomas allow therefore the estimation and the characterization of flow properties of fine powders using plastic repulsion coefficient (κ_{pl}) and elastic–plastic contact consolidation coefficient (κ), which are both related to the particles material characteristics. Thus, for a softer material and for fine particles, the contact consolidation coefficient will be higher in magnitude ($\kappa_{pl} \rightarrow 1$) as compared to those for a harder material and for coarser particles ($\kappa_{pl} \approx 0$). Similarly, the elastic–plastic contact consolidation coefficient is expected to increase with increasing interparticle adhesive forces. As a result, values of these coefficients estimated by means of powder shear tests can be used to understand the flow behaviour of powders.

With the aim of analysing the powder flowability, Tomas proposed to estimate the material characteristic parameters using the concept of stationary yield locus (SYL), which is completely described by the parameters shown in Figure 3: the angle of internal friction (ϕ_i), the steady-state angle of internal friction (ϕ_{st}), the isostatic tensile strength of unconsolidated powder (σ_0), the centre and the radius of the Mohr circle for the steady-state flow ($\sigma_{M,st}$ and $\sigma_{R,st}$ respectively). While the standard yield loci (YL) describe the limits of incipient plastic deformation during consolidation and flow, the stationary yield locus (SYL) is the envelope of Mohr circles for steady-state flow with a certain negative intersection of the abscissa σ_0.

This steady-state yield locus is expressed in radius stress-centre stress coordinates as follows:

$$\sigma_{R,st} = \sin \phi_{st} \left(\sigma_{M,st} + \sigma_0\right) \tag{17}$$

The steady-state angle of internal friction is related to the increase in adhesive forces as a result of elastic–plastic contact deformation of particles ($\phi_{st} - \phi_i$). The larger difference

between these friction angles entails the softer particle contacts and consequently the more cohesive powder.

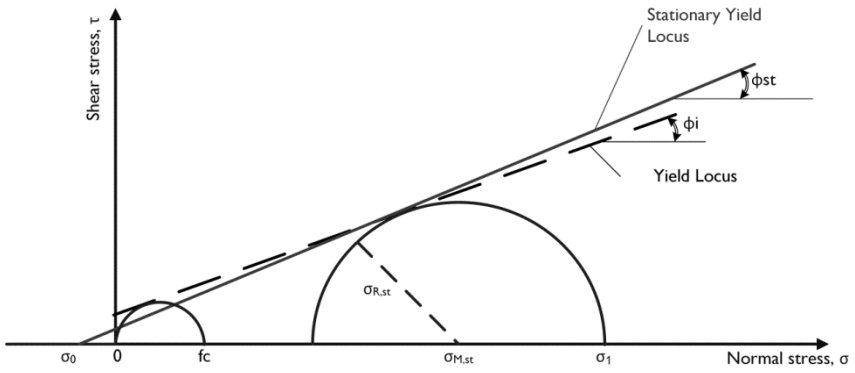

Figure 3 – Evaluation of steady-state yield locus and associated parameters

The centre and radius of the Mohr circle for the steady-state flow are invariants of the state of stress and are related to the pre-consolidation state and thus to the powder bulk density. They are calculated using the major and minor principal stresses (σ_1 and σ_2) from experimental yield loci data at each consolidation levels:

$$\sigma_{M,st} = \frac{\sigma_1 + \sigma_2}{2} \qquad \sigma_{R,st} = \frac{\sigma_1 - \sigma_2}{2} \tag{18}$$

Both ϕ_{st} and σ_0 can be estimated from the experimental flow function data (Molerus, 1975, 1978, 1994; Medhe et al., 2005):

$$f_c = \frac{2(\sin\phi_{st} - \sin\phi_i)}{(1+\sin\phi_{st})(1-\sin\phi_i)}\,\sigma_1 + \frac{2\sin\phi_{st}\,(1+\sin\phi_i)}{(1+\sin\phi_{st})(1-\sin\phi_i)}\,\sigma_0 \tag{19}$$

The contact consolidation coefficient κ can be then evaluated using Eqn. **(20)**:

$$\kappa = \frac{\tan\phi_{st}}{\tan\phi_i} - 1 \tag{20}$$

The isostatic tensile strength σ_0 of an unconsolidated powder having characteristic diameter d and without any particle contact deformation is related to the adhesion force F_{H0} by Eqn. (21) proposed by Molerus (1978):

$$\sigma_0 = \frac{F_{H0}}{d^2}\frac{1-\varepsilon_0}{\varepsilon_0} \tag{21}$$

The initial porosity ε_0 of loose packing needs to be considered. In order to estimate it Tomas proposed a relationship between powder bulk density and applied normal stresses introducing a compressibility index n by extending analogies to the adiabatic gas law for isentropic compression. In particular, he proposed a differential equation for isentropic compressibility of a powder:

$$dS = 0 \rightarrow \frac{d\rho_b}{\rho_b} = n\frac{dp}{p} = n\frac{d\sigma_{M,st}}{\sigma_0 + \sigma_{M,st}} \quad \textbf{(22)}$$

In which the total pressure includes particle interaction $p = \sigma_0 + \sigma_{M,st}$. Eqn. (22) can used to obtain loose powder packing density $\rho_{b,0}$ and thus the initial porosity ε_0, if particles are considered to be interacting without an external consolidation stress ($\sigma_{M,st} = 0$):

$$\rho_{b,0} = \rho_b \left(\frac{\sigma_0}{\sigma_0 + \sigma_{M,st}}\right)^n \quad \textbf{(23)}$$

$$\varepsilon_0 = \frac{\rho_p - \rho_{b,0}}{\rho_p} \quad \textbf{(24)}$$

The compressibility index n lies between n = 0, i.e. incompressible stiff bulk material, and n = 1, i.e. the ideal (gas) compressibility index. Therefore, the author suggested the semi-empirical estimated values for n reported in Table 1 (for σ_1 = 1-100 kPa).

Table 1 - Semi-empirical estimation of compressibility index of powders (Tomas, 2000)

n index	Evaluation	Example	Flowability
0 – 0.01	Incompressible	Gravel	Free flowing
0.01 – 0.05	Low compressibility	Fine sand	Free flowing
0.05 – 0.1	Compressible	Dry powder	Cohesive
0.1 – 1	Very compressible	Moist powder	Very cohesive

Tomas (2000) proposed also a relationship between κ, the Jenike flowability factors ff_c (Jenike, 1962) and the angle of internal friction ϕ_i in order to extend the use of the coefficient κ for powder flowability characterization:

$$\kappa = \frac{1 + (2\,ff_c - 1)\sin\phi_i}{\tan\phi_i\,(2\,ff_c - 1 + \sin\phi_i)} \sqrt{\frac{1}{1 - \left(\frac{1 + (2\,ff_c - 1)\sin\phi_i}{2\,ff_c - 1 + \sin\phi_i}\right)^2}} - 1 \quad \textbf{(25)}$$

Table 2 shows directly the correlation between flowability and elastic-plastic contact consolidation coefficient for a typical angle of internal fraction of 30°. However, as reported by Medhe et al. (2005), the use of Eqn. (20) to evaluate κ instead of calculating it from Jenike's flow function and ϕ_i directly using Eqn. (25) allows to avoid any dependence on consolidation levels.

Table 2 - Flowability assessment and κ calculated by Eqn. (25) according to Tomas theory

Flowability factors ff_c	κ value	ϕ_{st} [°]	Evaluation	Examples
100 – 10	0.01 – 0.107	30.3 – 33	Free flowing	Dry fine sand
4 – 10	0.107 – 0.3	33 – 37	Easy flowing	Moist fine sand
2 – 4	0.3 – 0.77	37 – 46	Cohesive	Dry powder
1 – 2	0.77 - ∞	46 – 90	Very cohesive	Moist powder
< 1	∞	-	Non flowing	Hydrated powder

4. Materials and methods

A Schulze Ring Shear Tester RST-01 has been used as a reference apparatus (Schulze, 1994b) to characterize the flow properties of the materials at ambient and high (500 °C) temperature. A standard Type S cell has been used at ambient temperature, while, to perform measurements of the powder flow properties at high temperature the cell modified by Tomasetta et al. (2013) has been used. The materials used for the construction of the High Temperature-Annular Shear Cell (HT-ASC) allow a safe operation of the system up to 500 °C.

The experimental procedure used to evaluate the flow properties of the material follows the standard shear tests procedure proposed by Schulze (2007). After filling the bottom ring of the cell and positioning it on the desk of the Ring Shear Tester, thermocouples and cooling system were set and the lid and the weights for consolidation were placed. In order to achieve the desired operating temperature, before starting the shear experiment, heaters were activated and steady-state temperature conditions at the set level were reached. Tomasetta el al. (2013) demonstrated the equivalence of the experimental measurements performed by the modified and the original Schulze shear cell.

In the Schulze tester, the lid is held in place and the bottom trough rotates determining a shear plane inside the material. Two load cells measure the torque necessary to keep the lid in place. A normal stress to the shear plane is applied by loading the lid with a certain weight. The tester is provided with a system able to balance the lid weight and therefore the normal stress is calculated as the weight loaded defined by the cell surface. The shear stress is determined by the torque necessary to keep the lid in place and the surface of the shear plane.

The stress distribution inside a bulk solid is usually described combining Yield Locus and Mohr circles analysis. Generally, the standard yield locus is obtained by fitting the results of shear tests to linear approximations based on the Coulomb equation that allows determining the tensile strength σ_t as:

$$\sigma_t = \frac{C}{\tan \phi_i} \tag{26}$$

In the present case study, the tests were carried following the procedure proposed by Schulze (2007) for a major principal stress σ_1 in the range 1 – 2 kPa. Such low normal stress values were adopted in order to approach a consolidation state relevant to fluidised powders. In fact, fluidization experiments will be performed in future work of the present project.

Two different types of titanium dioxide powders (TiO_2, rutile phase) supplied by *Huntsman Pigments and Additives* were chosen as experimental materials. In particular a synthetic rutile powder (SR) and a natural rutile powder (NR) have been used. The properties of these materials are listed in Table 3, including particle densities, bulk densities and assembly porosities at ambient temperature, Sauter mean diameters (SMD or d_{sv}), particle size distributions by weight (PSD) and relative diameter spread (RDS). Bulk densities and assembly porosities were calculated from data supplied from the Schulze apparatus. SMD, PSD and RDS were determined by sieve analysis and the 16^{th}, the 50^{th} and the 84^{th} percentile sizes (d_{16}, d_{50} and d_{84} respectively) are reported. In particular, RDS is defined according to Geldart (1987) and it is used to compare the width of the size distribution of the powders provided for this work.

Table 3 - Samples main properties

Sample	ρ_p [kg/m³]	$\rho_{b\,(25°)}$ [kg/m³]	$\varepsilon_{(25°)}$ [-]	d_{16} [µm]	d_{50} [µm]	d_{84} [µm]	d_{sv}[µm]	RDS [-]
Synthetic Rutile (SR)	3200	1500	0.53	122	162	212	145	0.28
Natural Rutile (NR)	4200	2320	0.45	117	202	379	155	0.65

To analyse particle shapes and surfaces, optical microscope imaging of the samples was performed. The images from optical microscope in Figure 4 show a rough surface and reasonably regular shapes for the synthetic rutile particles and they confirm the fairly wide particle size distribution measured by sieves technique. Figure 5 shows the images acquired for natural rutile powders. The sample exhibited very irregular shapes and rather smooth surfaces. Furthermore, such images confirm the large PSD observed with the sieves analysis. The roughness of the SR powder and the irregular shapes of the NR powder suggested that the local curvature radii at the contact points were considerably lower than the mean particle radii.

Thermal Gravimetric Analysis (TGA) and Differential Thermal Analysis (DTA) were performed by a SDT-Q600 (TA Instruments) with the aim of assessing the occurrence of phase transitions or chemical reactions in the temperature range of interest. Figure 6 shows the heat flow and the sample weight as a function of temperature for the samples. Inspection of the heat flow plot reported in the figure reveals that melting or solid phase transitions do not occur in the temperature range investigated. Moreover, a weight loss lower than the 1 % occurred at around 500 °C, due to the loss of moisture present in the sample. Given the very limited weight changes, a constant weight of the sample can be reasonably considered and it allows excluding the occurrence of chemical reactions (e.g. oxidation).

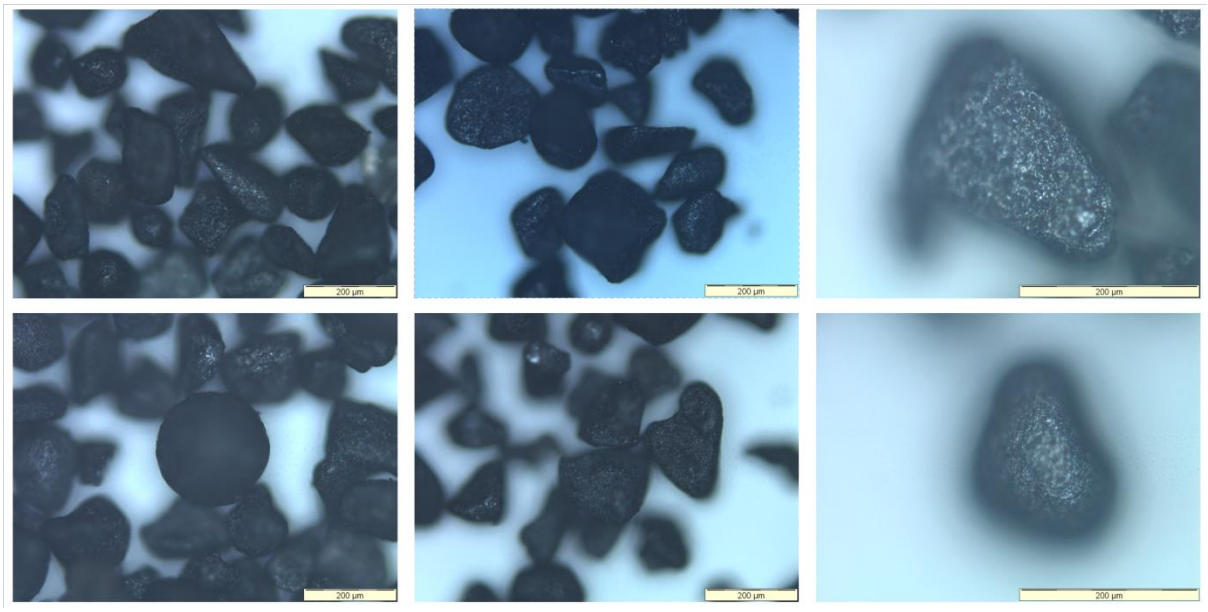

Figure 4 – Optical microscope images of synthetic rutile sample.

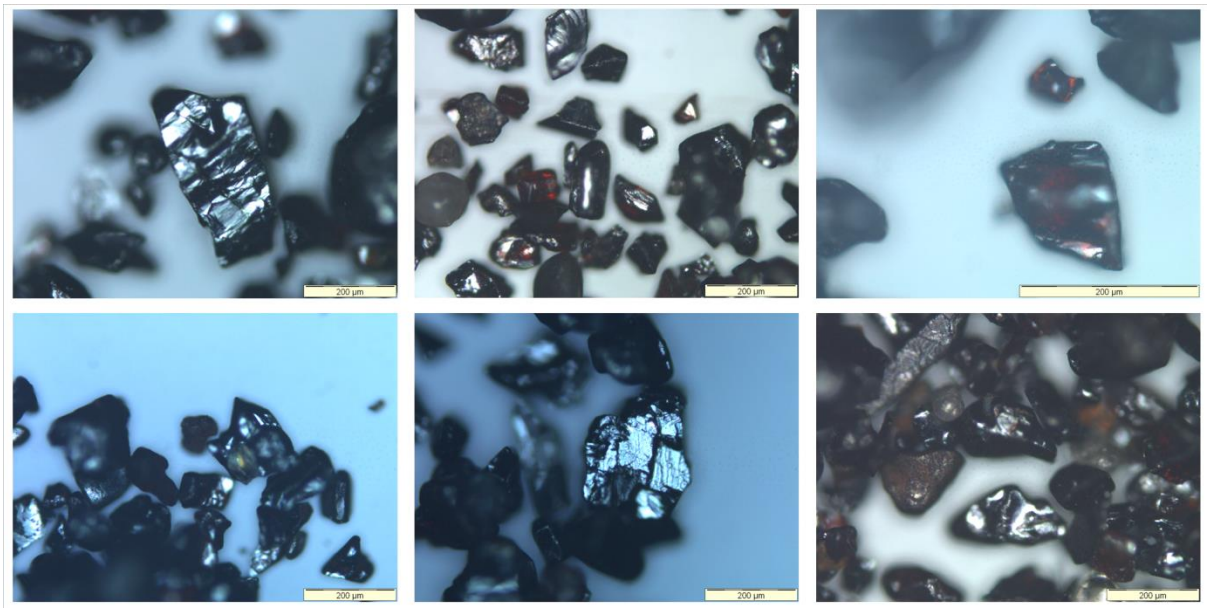

Figure 5 – Optical microscope images of natural rutile sample.

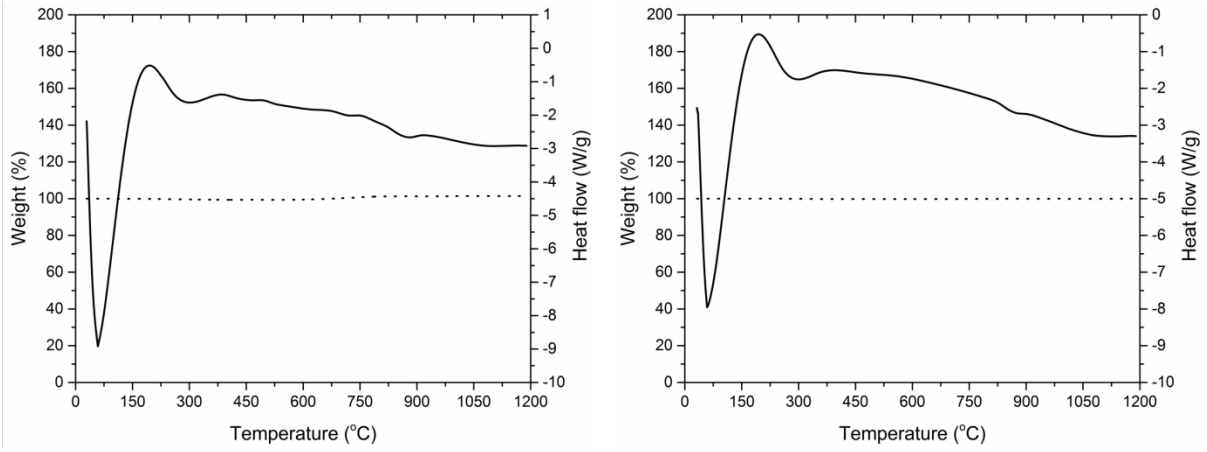

Figure 6 – TGA analysis for synthetic (left side) and natural (right side) rutile samples. Solid line is for heat flow and dotted line is for the weight variation.

5. Results and discussion

5.1 Experimental results

The yield loci and the flow functions of the two tested materials at ambient and high temperatures are reported in Figure 7. The main results in terms of major and minor principal stresses, consolidation stress, angle of internal friction, cohesion and tensile strength are listed in Table 4.

Table 4 - Results of the shear test performed with the Schulze apparatus

Sample	T (°C)	Cell Type	YL	σ_1 (Pa)	σ_2 (Pa)	σ_N (Pa)	C (Pa)	ϕ (°)	σ_t (Pa)	f_c (Pa)
Synthetic Rutile (SR)	25	S	1	986	261	571	4	35.2	5.7	16
			2	1200	310	696	5	35.9	6.9	19
			3	1409	369	820	5	35.5	7.0	21
			4	1633	431	944	6	35.3	8.5	25
	500	HT	1	982	263	564	31	32.5	48.7	112
			2	1215	310	688	33	34.0	48.9	126
			3	1435	352	812	35	35.1	49.8	135
			4	1689	414	936	40	35.2	56.7	153
Natural Rutile (NR)	25	S	1	1151	252	603	9	39.2	11.0	39
			2	1353	295	728	10	39.3	12.2	44
			3	1550	339	852	11	39.3	13.4	46
	500	HT	1	1055	271	590	16	34.8	23.0	61
			2	1264	322	714	17	35.3	24.0	65
			3	1502	363	838	18	36.6	24.2	72
			4	1728	428	962	20	36.1	27.4	79

The shear tests on the synthetic rutile powder were performed at low consolidation levels corresponding to major principal stresses in the range of approximately 1000 - 1700 Pa. The corresponding yield loci at different levels of consolidation for tests at ambient and high temperatures are reported in Figure 7(a) and Figure 7(b), respectively.

A slight change in the cohesion and therefore in the tensile strength were observed with increasing consolidation stress, both at ambient and high temperature. A slight upward shift in the yield loci was instead observed from ambient to high temperature for a given consolidation level. Such a shift corresponds to an increase of C from 5 $\pm$1 to about 34.8 $\pm$3 Pa and of σ_t from 7 $\pm$1 to 51 $\pm$3 Pa.

The tests on the natural rutile were performed at low consolidation levels as well, which correspond to the same range for major principal stresses of synthetic rutile. The corresponding yield loci at different levels of consolidation for tests at ambient and high temperatures are reported in Figure 7(c) and Figure 7(d), respectively. Also for this powder, slight changes in the cohesion and in the tensile strength were observed with increasing consolidation stress, both at ambient and high temperature. However, as observed for the synthetic rutile, a slight upward shift in the yield loci was observed from ambient to high

temperature for a given consolidation level, causing an increase of C from 10 ±1 to about 18 ±2 Pa and of σ_t from 12 ±1 to 25 ±2 Pa.

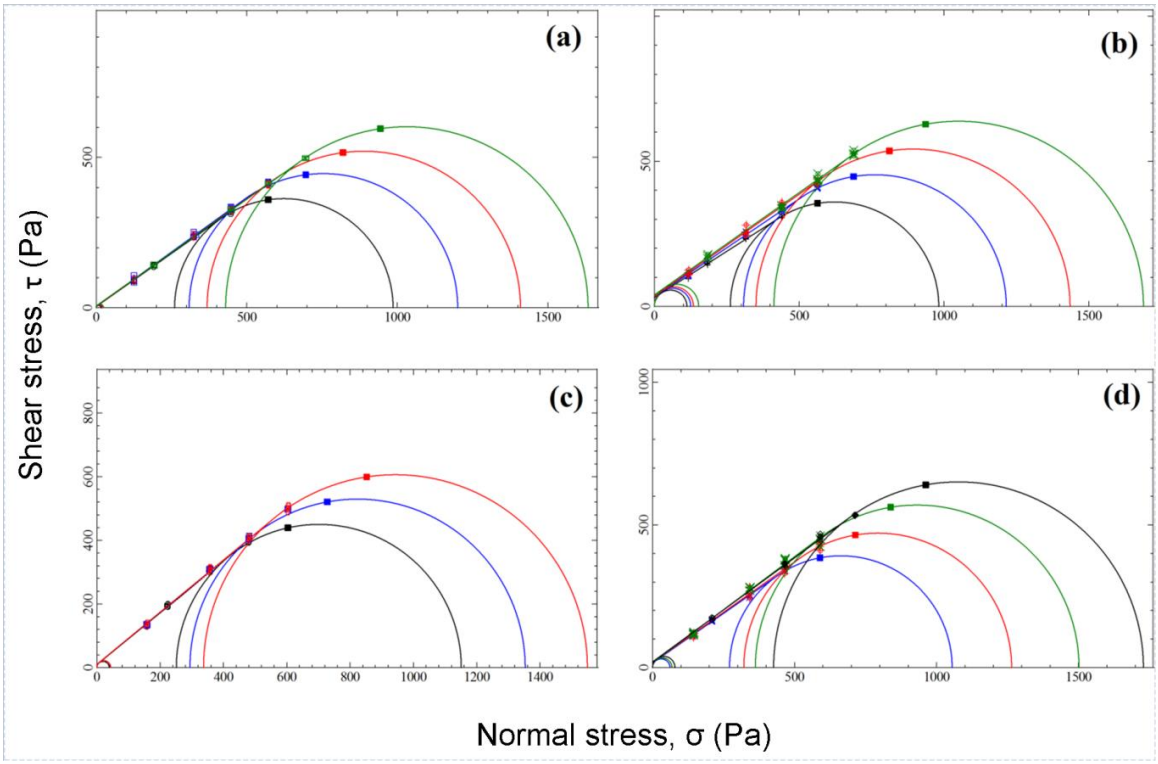

Figure 7 – Yield loci measured with the Schulze apparatus at ambient and high temperature and at different levels of consolidation. (a), (b) Synthetic rutile at 25 °C and 500 °C respectively. (c), (d) Natural rutile at 25 °C and 500 °C respectively. Filled symbols: experimental pre-shear data; hollow symbols: experimental shear data.

Figure 8 reports the flow functions of the three tested powder samples, according to Jenike's standard form and classification. The inspection of the figure shows how the powders flowability is slightly influenced by temperature in the range explored.

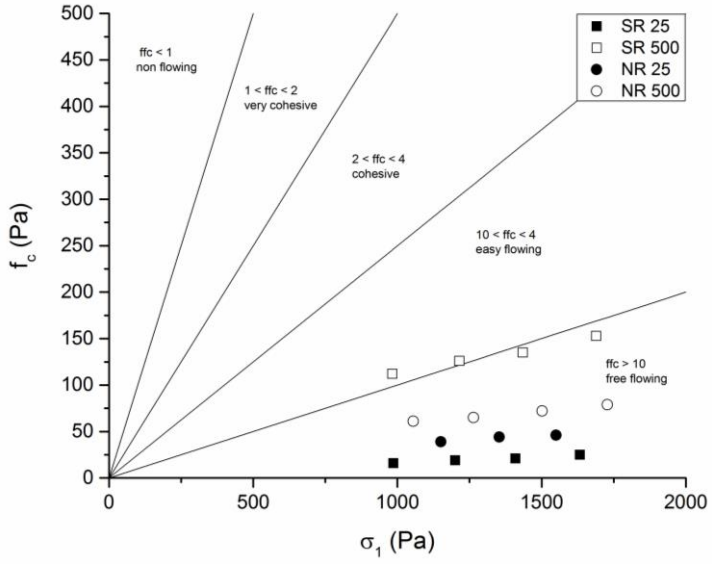

Figure 8 – Flow functions of the three tested powders measured with the Schulze apparatus at ambient and high temperatures.

5.2 Models results

With the aim to correlate the macroscopic powder flow properties with the forces that act between particles in the microscopic scale and to give an interpretation of the particle–particle contact mechanics a quantitative evaluation was performed.

Both theoretical models described in the previous section were implemented for this purpose. However, they show some problems due to the difficulty in identifying the accurate physical and mechanical properties of the materials at the different conditions investigated, such as the Hamaker constant, the compressive yield strength and the mean local curvature radius at the contact point.

Unique values of the Hamaker constant and of the characteristic molecular separation distance z_0 were assumed for both the samples and temperatures, according to the value reported by Tomas (2000) for titanium dioxide. Although, due to the thermal expansion and the thermal effects on mechanical properties of the particle material, different values of Young's modulus E (Wachtman et al., 1961; Soediono, 2009), particle densities ρ_p (Kirby, 1967) and compressive yield strength p_f (Guermazi et al., 1991; Tomas, 2000) were adopted at 25°C and 500°C, as well as of samples porosities and bulk densities, measured during shear tests with HT-ASC. The average main materials properties adopted in the present case study are listed in Table 5.

Table 5 - Samples main average properties

Sample	T [°C]	ρ_p [kg/m^3]	ρ_b [kg/m^3]	ε [-]	$C_{H,sfs}$ [10^{-20} J]	z_0 [nm]	E [GPa]	ν [-]	σ_f [MPa]	H_V [GPa]
Synthetic Rutile (SR)	25	3200	1500	0.53	12.6	0.336	284.2	0.28	130	10
	500	3120	1385	0.56	12.6	0.336	270.8	0.28	80	5
Natural Rutile (NR)	25	4200	2320	0.45	12.6	0.336	284.2	0.28	130	10
	500	4120	2050	0.50	12.6	0.336	270.8	0.28	80	5

With regard to the compressive yield strength p_f, it is necessary to consider that the local plastic deformation occurs under hindered conditions because of the surrounding material at the contact point. Hence, such a parameter is larger than the compressive yield strength usually measured under unhindered deformation conditions (σ_f) and reported in the literature. According to the theoretical works of Hencky (1923) and Ishlinsky (1944) and as reported by Tomasetta el al. (2014), the correct value for $p_f \approx 3\ \sigma_f$ should be considered. Moreover, σ_f values at high temperature are hard to find in the literature and the reported values are often ambiguous and controversial. As observed for similar materials (Frost and Ashby, 1982; Poirier, 1985; Weidner et al., 1994) the compressive yield strength was considered to decrease with temperature and it was estimated as:

$$p_{f,500} = \alpha\, p_{f,25} \quad \textbf{(27)}$$

Where α is a proportional constant varying in the range 0.1-1 that relates p_f at high temperature with the one at ambient temperature. However, in the present case study two approaches were followed:

- at first the value for the compressive yield strength at ambient conditions was considered equals to 400 MPa as reported by Tomas (2000) and an average values of $\alpha = 0.6$ was used;
- Secondly, the Vickers Hardness (H_V) of polycrystalline TiO_2 reported by Guermazi et al. (1991) as a function of temperature was considered as compressive yield strength.

The sample porosity ε was estimated from Eqn. (28), using the values of particle densities (from powders data sheets) and bulk densities measured by the Schulze cell, both reported in Table 5.

$$\varepsilon = 1 - \frac{\rho_p}{\rho_b} \quad \textbf{(28)}$$

This assessment is affected by some inaccuracies, because of the leakage of the powder from the cell during shear testing, as observed by Tomasetta et al. (2014). This leakage may entail an overestimation of the effective mass of the sample, and a resulting underestimation of the relevant porosity, which is calculated from the bulk density (i.e., the ratio between the initial sample mass and the current sample volume). Moreover, the estimated porosity is an averaged value and is not necessarily representative of the local porosity in the shear zone, which is more relevant to the measured stresses. In fact, powder dilation in the shear zone makes the local porosity value larger than the sample average. However, as reported by Tomasetta et al. (2014), changes in this parameter slightly affect the model results.

5.2.1 Rumpf-Molerus model results

In order to overcome the problem of identifying the accurate value of the compressive yield strength, the following procedure was followed:

- the model was first fitted by experiments values at both ambient and high temperature to determine the mean curvature radius r_{pl} (that is considered constant with temperature) at the reference properties reported in Table 5;
- sensitivity analysis was then performed to assess the effects of changes in compressive strength.

Experimental values of cohesion and angle of internal friction were used to estimate the powder tensile strength σ_t according to Eqn. (26). Such a value was compared with the tensile strength values obtained by the application of the models σ_t^*.

For each sample, the value of r_{pl} that best fits the estimated tensile strengths to the experimental value was calculated. It was estimated by minimizing the mean square error (MMSE method) between the tensile strength evaluated from experimental data and the predicted values calculated by combining Eqn. (2) and (16), using data for each consolidation level. The value for the normal consolidation force F_N required by Eqn. (16) was estimated with Eqn. (11), using as consolidation stress $\sigma_N = \sigma_{pre}$, i.e. the normal stress for pre-shear phase. As discussed above, it is reasonable to extend Eqn. (11) to a real consolidation state for stress, which is generally applied for an isostatic state of stress, for limited tangential forces on the plane of interest.

The results obtained by the application of the Rumpf-Molerus mathematical models for each material with the reference properties reported in Table 5 are reported in Table 6. They seem to agree with the features observed with the optical microscope imaging, they are dependent on both the contact model and the reference p_f value.

Table 6 - Main results of the Rumpf-Molerus mathematical models

Sample	T [°C]	F_N [μN]	p_f from Tomas (2000)					p_f from Guermazi et al. (1991)				
			r_{pl} [μm]	κ_{pl} [-]	F_0 [pN]	F_H [μN]	σ_t^* [Pa]	r_{pl} [μm]	κ_{pl} [-]	F_0 [nN]	F_H [μN]	σ_t^* [Pa]
Synthetic Rutile	25	13.99	0.7×10^{-6}	0.79	0.115	11.0	449.6	2.1	0.02	196	0.45	18.2
		16.54				13.0	548.1				0.49	20.7
		19.59				15.4	645.7				0.55	22.9
		22.33				17.6	743.4				0.60	25.2
	500	15.09		2.76	0.241	41.7	1558.2		0.04	200	0.75	28.1
		18.22				50.3	1900.8				0.87	32.7
		21.31				58.9	2243.4				0.98	37.3
		24.28				67.1	2586.0				1.09	41.9
Natural Rutile	25	11.91	0.6×10^{-6}	0.79	0.092	9.4	474.8	4.8×10^{-3}	0.02	0.45	0.21	10.8
		14.17				11.2	573.3				0.25	13.1
		16.36				12.9	670.9				0.29	15.3
	500	14.50		2.76	0.194	40.1	1630.1		0.04	0.46	0.53	21.6
		17.33				47.9	1972.7				0.63	26.1
		20.06				55.4	2315.3				0.73	30.6
		23.29				64.4	2657.9				0.85	35.2

In order to perform the MMSE, the Matlab routine FMINCON was used. This routine is based on the method of Lagrange multipliers, which enables to solve general minimization problems subjected to constraints. In this case, the problem consists in finding the value of r_{pl} which corresponds to the minimum value for MSE. This problem is subjected to one

constraint only: the value of the local curvature radius must be greater than zero and less than the mean particle radius, i.e. $d_{50}/2$.

The model results also confirm the expectations on the low local curvature radii compared to the particle size. In particular for the SR powder, the curvature radius at the contact point was expected to be on the order of the particle roughness (Bennett et al., 1989; Ritala et al., 1994).

Results in terms of interparticle forces, tensile strength and other model parameters are reported in Table 6, where the values obtained with the two different approaches are also presented. The tensile strength values obtained by the application of the model σ_t^* are compared with the tensile strength values calculated from experimental data σ_t in Table 7.

Table 7 - Comparison of tensile strength values obtained from Rumpf-Molerus models versus values obtained from experimental data

	Synthetic Rutile			Natural Rutile		
T [°C]	σ_t [Pa]	$\sigma^*_{t,Tomas}$ [Pa]	$\sigma^*_{t,Guermazi}$ [Pa]	σ_t [Pa]	$\sigma^*_{t,Tomas}$ [Pa]	$\sigma^*_{t,Guermazi}$ [Pa]
25	5.7	449.6	18.2	11.0	474.8	10.8
25	6.9	548.1	20.7	12.2	573.3	13.1
25	7.0	645.7	22.9	13.4	670.9	15.3
25	8.5	743.4	25.2	-	-	-
500	48.7	1558.2	28.1	23.0	1630.1	21.6
500	48.9	1900.8	32.7	24.0	1972.7	26.1
500	49.8	2243.4	37.3	24.2	2315.3	30.6
500	56.7	2586.0	41.9	27.4	2657.9	35.2

It can be clearly seen that Rumpf -Molerus model do not fit properly with the experimental data in the case in which the value of p_f proposed by Tomas is taken into account. The model shows great discrepancies with the experimental evidences maybe because of the unsuitable value for the compressive strength considered. In fact, as discussed before, this is one of the key parameters of the Rumpf-Molerus modelling approach; values at both ambient and high temperatures are difficult to find in the literature and they are often ambiguous and controversial. On the other hand, in the case when $p_f = H_V$ is considered, the model gives reasonable estimates of tensile strength values at both investigated temperatures for all the samples tested. These results confirm that such a model approach might deliver a relationship between the experimental tensile strength and its theoretical prediction with a correct order of magnitude estimated, if reasonable values for the compressive yield strength and the curvature of the particle surface are taken into account.

As indicated previously, the sensitivity of the model to the compressive yield strength at both ambient ($p_{f,25}$) and high temperature ($p_{f,500}$) was carried out. In particular, values for $p_{f,25}$

in the range between 0.08 and 31.6 GPa and different values for the parameter α in Eqn. (27) have been considered.

The results for the SR sample are shown in Figure 9 where the ratio σ_t^*/σ_t, i.e. the ratio between the tensile strength obtained from Rumpf-Molerus model and the one calculated from experimental data, is reported as function of compressive yield strength. The sensitivity analysis suggests relevant effect on the ratio σ_t^*/σ_t for variations of both $p_{f,25}$ and α. It can be seen that such a ratio is closer to 1 for values of the compressive strength at ambient temperature higher than the reference ones and for values of α lower than 0.6. In particular, the best fitting between model and experimental data is obtained when the value of α is in the range 0.1 - 0.2 and if values for $p_{f,25}$ from 15 to 20 GPa are considered. Furthermore, the tensile strengths of yield loci at high temperature are less influenced by changes in $p_{f,25}$ and α than the ones of the yield loci at ambient temperature.

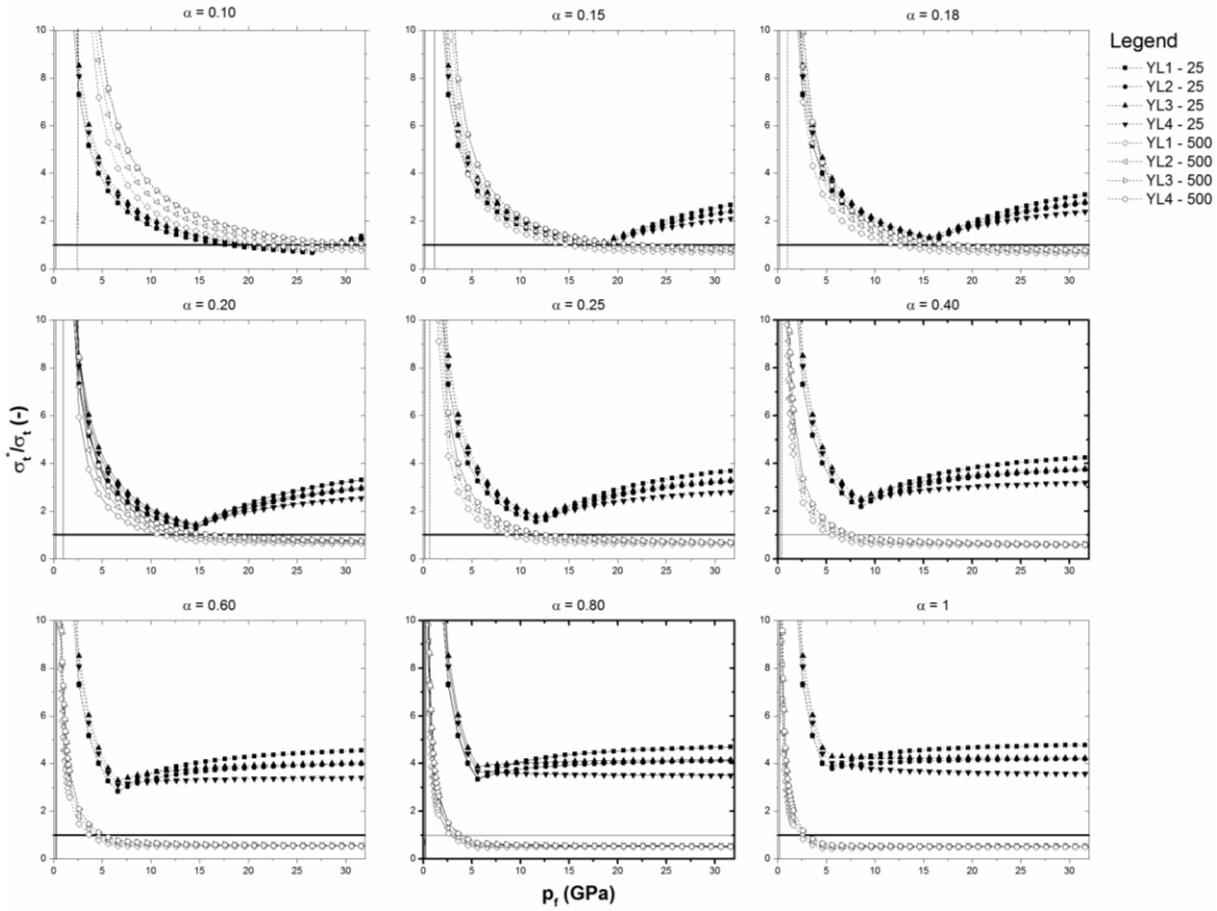

Figure 9 – Scatter plot of the ratio between the tensile strength obtained from Rumpf-Molerus model and the tensile strength calculated from experimental data versus changes in compressive strength for SR sample: sensitivity analysis for p_f at ambient temperature (on the abscissas axis) and for p_f at high temperature (graphs parametric with α).

The results for the NR samples are shown in Figure 10. The sensitivity analysis suggests major effects on the tensile strength. The ratio σ_t^*/σ_t follows similar trends as those of

synthetic rutile. The best fitting between model and experimental data is obtained when $p_{f,25}$ is in the range 10 - 20 GPa and if values of α from 0.30 to 0.60 are considered.

Thus, the sensitivity analysis shows that the Rumpf-Molerus model approach might provide a good estimate for the theoretical tensile strength if a reasonable value for the compressive yield strength is taken into account. Furthermore, considering accurate changes in p_f with temperature can explain the temperature effects on the tensile strength observed during the experiments. In fact, a change in the adopted value of α (and then of $p_{f,500}$) could improve the fitting of the model data with the experimental ones for all evaluated temperatures.

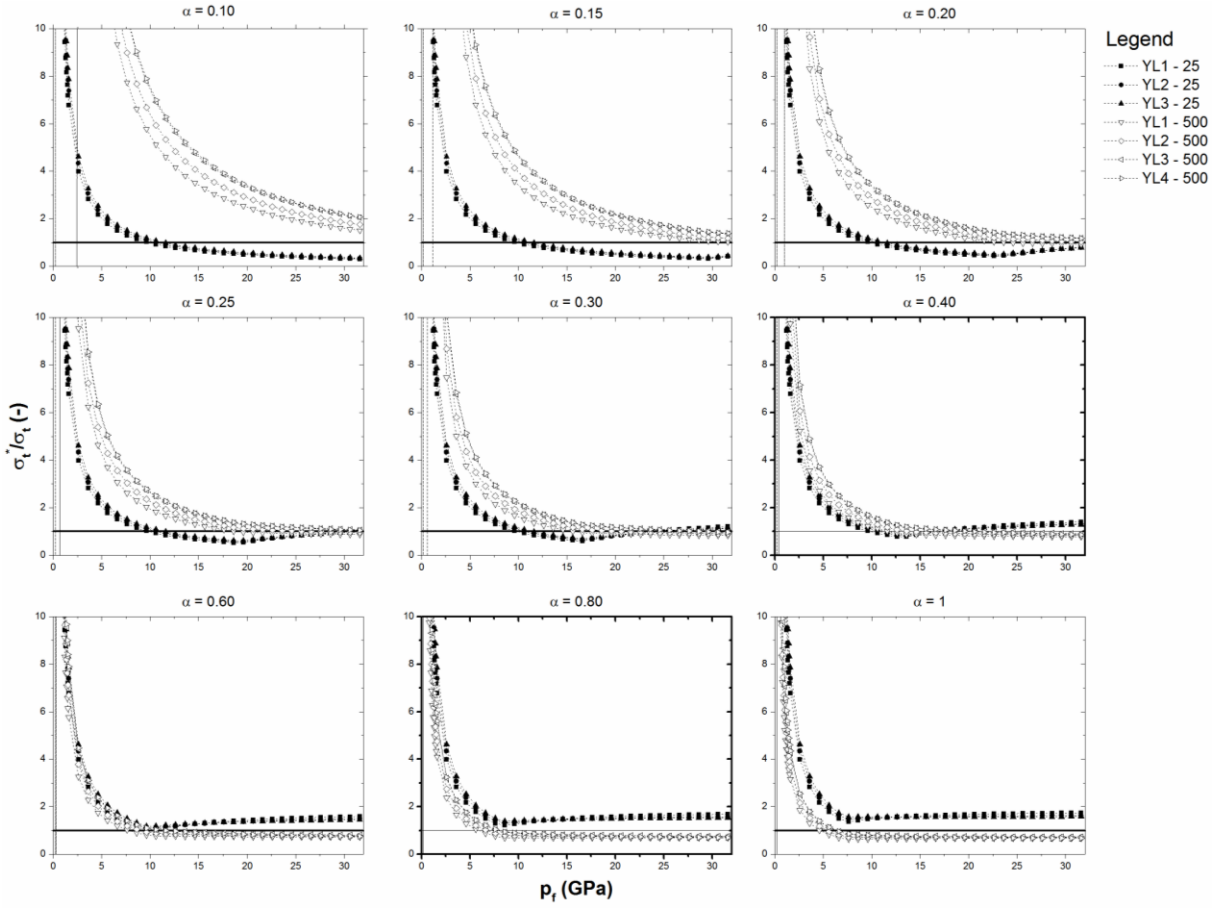

Figure 10 - Scatter plot of the ratio between the tensile strength obtained from Rumpf-Molerus model and the tensile strength calculated from experimental data versus changes in compressive strength for NR sample: sensitivity analysis for p_f at ambient temperature (on the abscissas axis) and for p_f at high temperature (graphs parametric with α).

5.2.2 Tomas model results

The results obtained from the application of the mathematical model proposed by Tomas are reported in Table 8, in which interparticle forces, mean tensile strength and models parameters are presented.

The κ values obtained from the application of Eqn. (9) as slope of the linear relationship between experimental F_H and F_N are also reported and compared with the values obtained from Eqn. (20). The material characteristic parameters of SYL that allowed the estimation of κ^* from Eqn. (20) are presented as well. They were estimated combining Eqns. (17) - (19) as shown in the flowchart in Figure 11.

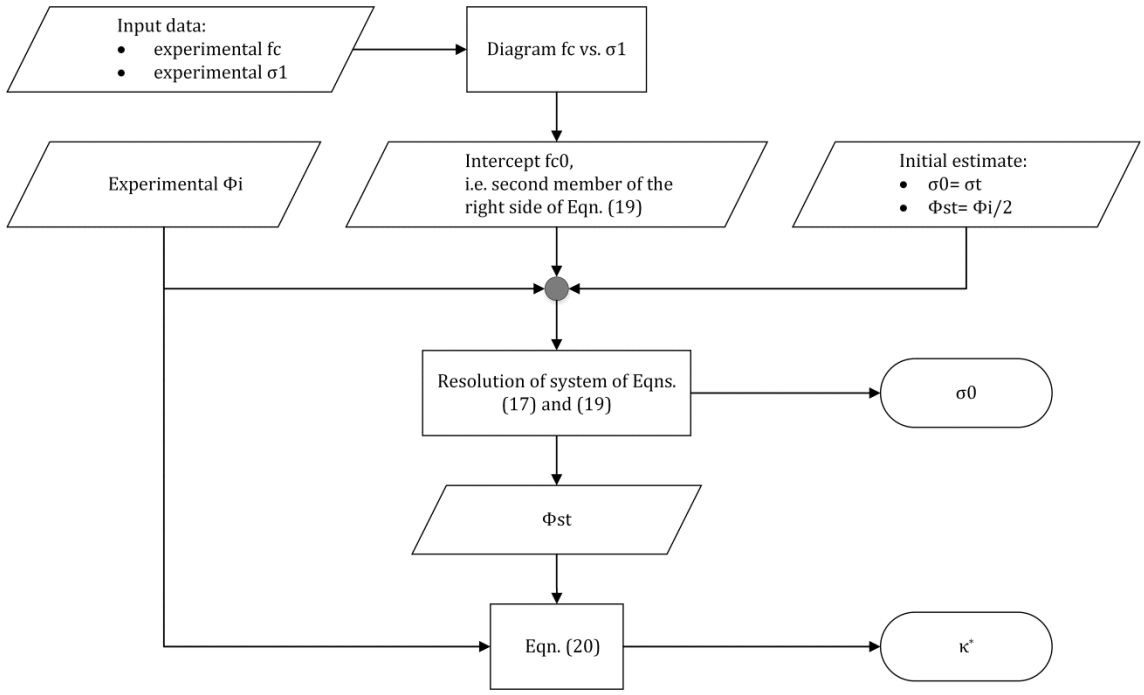

Figure 11 – Flowchart showing the calculation process for κ* and σ_0

Despite the significant number of simplifying assumptions that were considered, the model gives reasonable estimates of κ values at both investigated temperatures. It is also important to note that the estimation of κ* and σ_t* is independent of the compressive yield strength. More details about the fitting analysis on the experimental F_H vs. F_N data are reported in Table 9.

The parameters for the evaluation of initial porosity ε_0 according to Eqns. (23) and (24) are reported in Table 10. The compressibility index n was estimated according to Tomas suggestions reported in Table 1. This index was related to the flowability assessments discussed in Table 2 for κ values. In the present case study, the κ values for all the samples are in the range of 0.01 – 0.107, so an n index of 0.01 was considered.

Figure 12 shows the comparison between the tensile strength values obtained by the application of the model and the experimental values. Even though the model seems to overestimate tensile strength value by 20%, a quite good match is reached between model and experimental values.

Table 8 - Main results of the Tomas mathematical models

Sample	T [°C]	F_N [nN]	κ [-]	Model results				SYL parameters		
			F_H-F_N slope	κ^* [-]	F_{H0} [nN]	F_H [nN]	σ_t^* [Pa]	ϕ_{st} [°]	σ_0 [Pa]	$\sigma_{M,st}$ [Pa]
Synthetic Rutile	25	13987	0.007	0.010	26	166	6.8	35.5	0.95	624
		16543			25	190	8.0	36.1	0.91	755
		19588			25	221	9.3	35.8	0.93	889
		22325			26	249	10.5	35.6	0.94	1032
	500	15089	0.017	0.048	666	1429	53.4	33.8	23.70	623
		18217			612	1523	57.5	35.2	21.75	763
		21306			574	1634	62.3	36.3	20.41	894
		24276			570	1773	68.4	36.5	20.28	1052
Natural Rutile	25	11910	0.009	0.011	121	248	12.6	39.5	5.58	702
		14173			120	271	13.9	39.6	5.55	824
		16365			120	295	15.3	39.6	5.55	945
	500	14498	0.010	0.022	311	634	25.8	35.5	11.78	663
		17328			303	687	28.3	35.8	11.48	793
		20064			281	724	30.2	37.1	10.64	933
		23295			289	803	33.2	36.6	10.95	1078

Table 9 - Output data from linear fitting

	Intercept		Slope		Statistics		
	Value	Stand. Error	Value	Stand. Error	Adj. R-Square	Res. sum of Squares	Pearson's r
SR25	4.74E-08	2.72E-08	0.007	0.001	0.864	1.73E-16	0.954
SR500	1.01E-06	1.89E-07	0.017	0.009	0.415	8.41E-15	0.781
NR25	1.10E-07	1.89E-09	0.009	0.000	0.999	1.74E-19	1.000
NR500	4.05E-07	7.96E-08	0.010	0.004	0.628	1.48E-15	0.867

Table 10 - Evaluation of bulk powders initial conditions

Sample	T [°C]	κ* value	n	ε_0 [-]	$\rho_{b,0}$ [kg/m³]
Synthetic Rutile	25	0.010	0.01	0.56	1398
	500	0.048	0.01	0.57	1336
Natural Rutile	25	0.011	0.01	0.47	2207
	500	0.022	0.01	0.52	1965

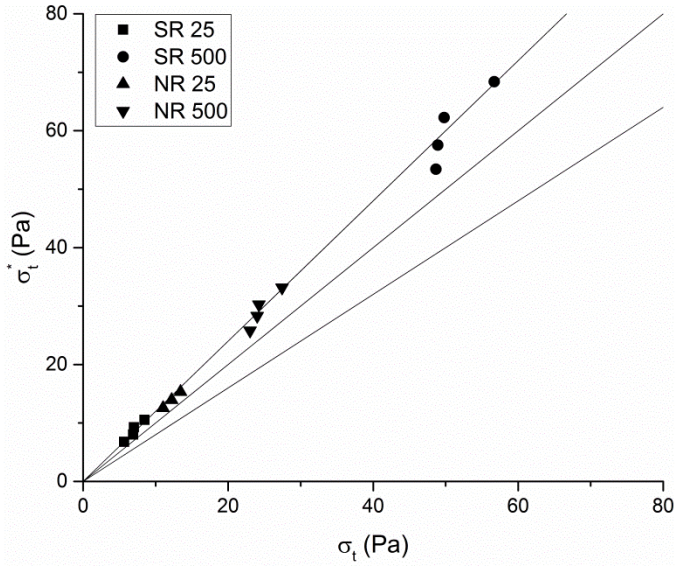

Figure 12 – Parity plot of tensile strength values obtained from Tomas model versus values obtained from experimental data.

In addition, the κ values were evaluated according to Eqn. (10), as shown in Table 11. To this end the coefficients κ_P and κ_A were estimated by Eqns. (5) and (6) and material properties reported in Table 5. The calculated displacement h_c is also reported in Table 11. The calculation process for κ^{**} and h_c is shown in the flowchart in Figure 13.

As for Rumpf-Molerus model, the Tomas approach for the calculation of the deformation displacement is strongly dependent on the value of compressive yield strength considered. In the present analysis both Tomas (2000) and Guermazi et al. (1991) proposals for p_f were firstly considered, while a sensitivity analysis on such parameters was then carried out.

Table 11 - First evaluation of κ^{**} values according to Eqn. (10)

Sample	YL	T [°C]	p_f from Tomas (Tomas, 2000)				p_f from Guermazi et al. (Guermazi et al., 1991)			
			κ_P	κ_A	κ^{**}	h_c [nm]	κ_P	κ_A	κ^{**}	h_c [nm]
Synthetic Rutile	1	25	0.441	0.726	1.545	1.08	0.018	1.00	0.018	0.013
	2	25	0.441	0.737	1.487	1.22	0.018	1.00	0.018	0.015
	3	25	0.441	0.748	1.431	1.40	0.018	1.00	0.018	0.018
	4	25	0.441	0.757	1.393	1.55	0.018	1.00	0.018	0.020
	1	500	0.734	0.872	5.338	4.19	0.035	1.00	0.036	0.029
	2	500	0.734	0.877	5.126	4.81	0.035	1.00	0.036	0.034
	3	500	0.734	0.882	4.962	5.41	0.035	1.00	0.036	0.040
	4	500	0.734	0.886	4.834	5.99	0.035	1.00	0.036	0.045
Natural Rutile	1	25	0.441	0.705	1.663	0.93	0.018	1.00	0.018	0.010
	2	25	0.441	0.718	1.589	1.06	0.018	1.00	0.018	0.012
	3	25	0.441	0.728	1.534	1.18	0.018	1.00	0.018	0.014
	1	500	0.734	0.865	5.602	3.87	0.035	1.00	0.036	0.025
	2	500	0.734	0.871	5.368	4.40	0.035	1.00	0.036	0.030
	3	500	0.734	0.876	5.188	4.93	0.035	1.00	0.036	0.035
	4	500	0.734	0.880	5.024	5.52	0.035	1.00	0.036	0.040

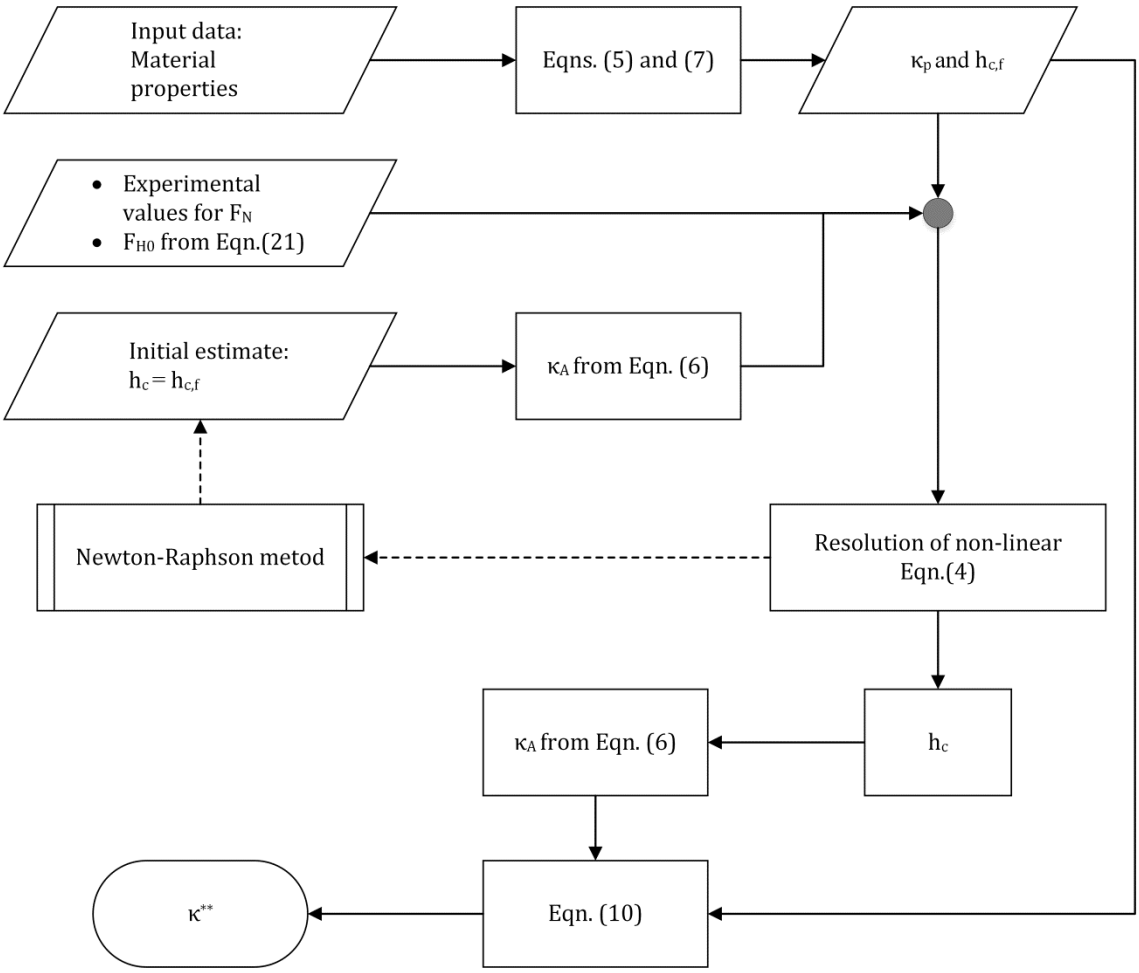

Figure 13 – Flowchart showing the calculation process for κ**

The sensitivity analysis on the elastic-plastic consolidation coefficient as function of $p_{f,25}$ for materials at ambient temperature is reported in Figure 14, while the effects of $p_{f,25}$ and α on κ^{**} for materials at high temperature are instead described in Figure 15.

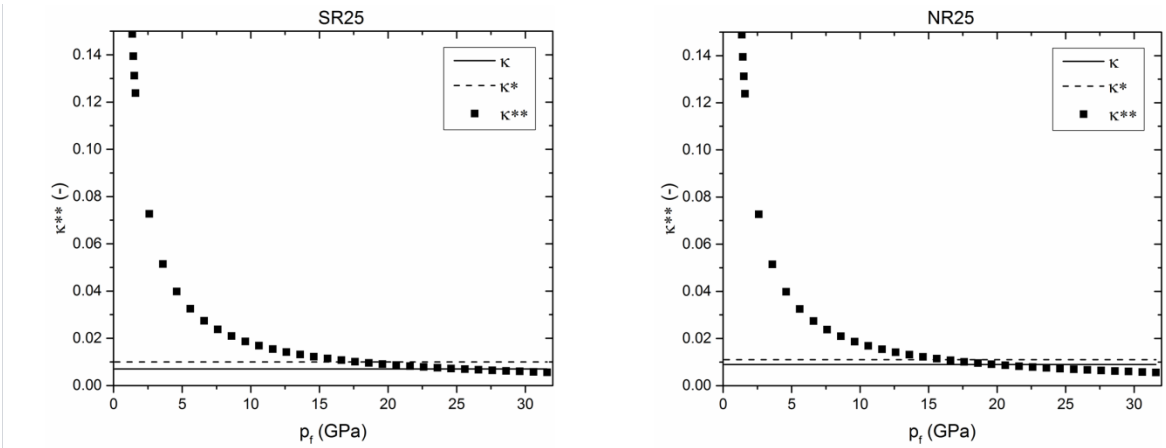

Figure 14 – Sensitivity analysis on κ^{**} as function of $p_{f,25}$

As shown in Figure 14, the sensitivity analysis for samples at ambient temperature suggests relevant effect on the consolidation coefficient for variations of $p_{f,25}$. It shows that

κ^{**} is closer to κ^{*} and κ values for compressive strengths different from the reference ones. In particular, for both the materials the best fitting is achieved if values of $p_{f,25}$ higher than 18 GPa are considered.

The results at high temperature suggest major effects on the elastic-plastic consolidation coefficient for variations of both $p_{f,25}$ and α. The sensitivity analysis shows that the coefficient κ^{**} follows the same trend in both cases regarding changes of $p_{f,25}$ and α: it decrease with increasing compressive yield strength and α values.

However, the best fitting between the values of the three consolidation coefficients depends on the inspected material. In the case of synthetic rutile, the analysis shows different matches between κ^{**} and κ^{*} and between κ^{**} and κ in relation to the couple $p_{f,25}$ - α considered. In particular, the matches between κ^{**} and κ^{*} range from 4 to 20 GPa for $p_{f,25}$ and from 0.2 to 1 for α. Whereas, the matches between κ^{**} and κ are achieved for $p_{f,25}$ = 10 - 30 GPa and α = 0.4 – 1. On the other hand, for the natural rutile the analysis suggests as best match with κ^{*} $p_{f,25}$ = 8 – 30 and α = 0.3 – 1; and with κ $p_{f,25}$ = 15 – 30 and α = 0.5 – 1.

Therefore, similarly to the theoretical model proposed by Rumpf and Molerus, the sensitivity analysis shows that the Tomas modelling approach might provide good estimates of consolidation coefficient and theoretical tensile strength if reasonable values for the compressive yield strength are taken into account. Moreover, considering accurate changes in p_f with temperature might explain the temperature effects observed during the experiments. In fact, a change in the adopted values of p_f and α could improve the fitting of the model data with the experimental ones for all the evaluated temperatures.

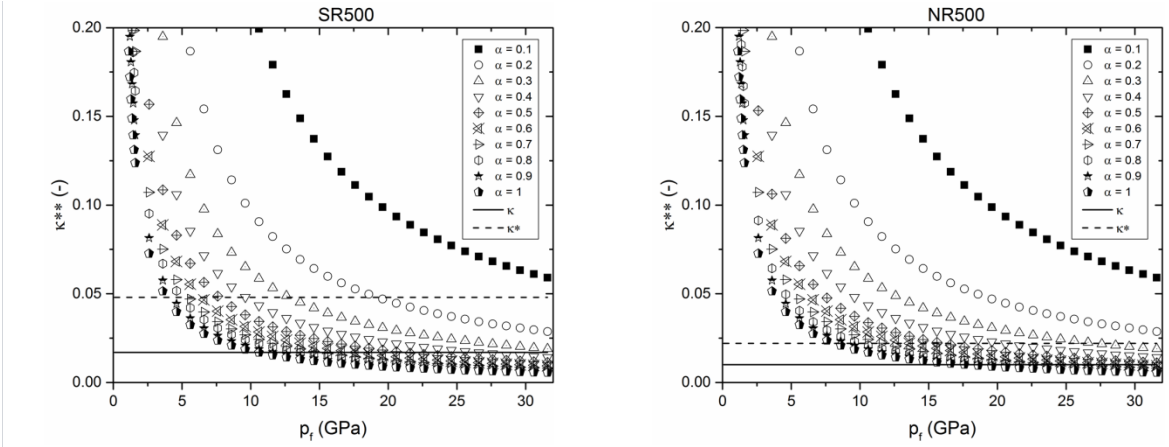

Figure 15 – Sensitivity analysis on κ^{**} as function of pf,25 and α

6. Conclusion

Experimental examinations with Schulze shear cell were carried out in order to assess the rheological behaviour of the materials at ambient and with increasing temperature. Shear experiments highlighted a significant increase of unconfined yield strength with temperature, which means that a higher force is required to deform or break the material when it is not confined by a container. From the particulate material perspective, it means that a higher force is required to fail a consolidated mass of material to initialize flow. This resulted in a lower flowability of the samples.

Theoretical models based on the particle–particle approaches of Rumpf and Molerus and of Tomas were used to correlate the isostatic tensile strength of powders with the interparticle interaction forces. The comparison between experiments conducted at ambient and high temperatures and the theoretical model suggests that the proposed approaches give correct predictions for the tensile strength if the proper values for the material physical and mechanical properties, in particular for the compressive yield strength, at both ambient and high temperature are used. In fact, as highlighted by the sensitivity analysis, different p_f values may yield better fits to the experimental data.

7. Acknowledgments

The authors acknowledge the technical and financial support from *Huntsman Pigments and Additives* and from the Faculty of Engineering Sciences at UCL.

8. Appendix A - Normal force-displacement function of particle contact

Tomas developed a normal force-displacement model starting from the particle contact forces equilibrium between attraction (-) and elastic plus simultaneous plastic repulsion (+) (r_c contact radius and r coordinate of annular elastic contact area):

$$\sum F = 0 = -F_{H0} - p_{VdW}\,\pi\,r_c^2 - F_N + p_f \pi\,r_{pl}^2 + 2\pi \int_{r_{pl}}^{r_c} p_{el}(r)\,r\,dr \qquad \textbf{(A1)}$$

Considering that, according to Hertz (1881) for a single elastic contact of two spheres 1 and 2 with a maximum contact circle radius r_c but small compared with the particle diameter d_1 and d_2, an elliptic pressure distribution $p_{el}(r)$ is assumed:

$$\left(\frac{p_{el}}{p_{max}}\right)^2 = 1 - \left(\frac{r}{r_c}\right)^2 \qquad \textbf{(A2)}$$

With the maximum pressure $p(r = 0) = p_{max}$ in the centre of contact circle:

$$p_{max} = \frac{3\,F_N}{2\,\pi\,r_{el}^2} \qquad \textbf{(A3)}$$

According to Eqn. (A2) the integral in Eqn. (A1) can be calculated as:

$$\int_{r_{pl}}^{r_c} p_{el}(r)\,r\,dr = \int_{r_{pl}}^{r_c} p_{max}\left(1 - \left(\frac{r}{r_c}\right)^2\right)^{\frac{1}{2}} r\,dr \qquad \textbf{(A4)}$$

And the solution is:

$$\int_{r_{pl}}^{r_c} p_{max}\left(1 - \left(\frac{r}{r_c}\right)^2\right)^{\frac{1}{2}} r\,dr = \frac{p_{max}\,r_c^2}{3}\left(1 - \left(\frac{r_{pl}}{r_c}\right)^2\right)^{\frac{3}{2}} \qquad \textbf{(A5)}$$

However, at the yield point $r = r_{pl}$ the maximum contact pressure reaches the yield strength $p_{el} = p_f$ and according to Hertz pressure distribution:

$$1 - \left(\frac{r_{pl}}{r_c}\right)^2 = \left(\frac{p_f}{p_{max}}\right)^2 \qquad \textbf{(A6)}$$

That leads to:

$$\frac{p_{max}\, r_c^2}{3}\left(1-\left(\frac{r_{pl}}{r_c}\right)^2\right)^{\frac{3}{2}} = \frac{p_{max}\, r_c^2}{3}\left(\frac{p_f}{p_{max}}\right)^3 = \frac{p_{max}\, r_c^2}{3}\left(\frac{p_f}{p_{max}}\right)\left(\frac{p_f}{p_{max}}\right)^2 = \frac{p_{max}\, r_c^2}{3}\left(\frac{p_f}{p_{max}}\right)\left(1-\left(\frac{r_{pl}}{r_c}\right)^2\right) = \frac{p_f\, r_c^2}{3}\left(1-\left(\frac{r_{pl}}{r_c}\right)^2\right) \quad \textbf{(A7)}$$

And so, the equilibrium of the contact forces can be expressed as:

$$F_{H0} + p_{VdW}\,\pi\, r_c^2 + F_N = p_f\left(\pi\, r_{pl}^2 + \frac{2\pi\, r_c^2}{3}\left(1-\frac{r_{pl}^2}{r_c^2}\right)\right) \quad \textbf{(A8)}$$

Finally, the contact force equilibrium:

$$F_{H0} + p_{VdW}\,\pi\, r_c^2 + F_N = \pi\, r_c^2 p_f\left(\frac{r_{pl}^2}{r_c^2} + \frac{2}{3}\left(1-\frac{r_{pl}^2}{r_c^2}\right)\right) = \pi\, r_c^2 p_f\left(\frac{2}{3} + \frac{1}{3}\frac{r_{pl}^2}{r_c^2}\right) \quad \textbf{(A9)}$$

And, if the total contact area A_c and the plastic contact deformation area A_{pl} are defined as:

$$A_c = \pi\, r_c^2 \quad \textbf{(A10)}$$

$$A_{pl} = \pi\, r_{pl}^2 \quad \textbf{(A11)}$$

Eqn. (A9) can be written as:

$$F_{H0} + F_N = A_c\, p_f\left(\left(\frac{2}{3} + \frac{1}{3}\,\frac{A_{pl}}{A_c}\right) - \frac{p_{VdW}}{p_f}\right) \quad \textbf{(A12)}$$

Next, the dimensionless coefficients κ_p and κ_A defined with Eqns. (5) and (6) are introduced in Eqn. (A12):

$$F_{H0} + F_N = A_c\, p_f\left(\kappa_A - \kappa_p\right) = \pi\, r_c^2\, p_f\left(\kappa_A - \kappa_p\right) \quad \textbf{(A13)}$$

Now, according to Tomas (2003), the surface displacement can be considered out of the contact zone and the height of overlap of both particles h_c can be related to the contact radius and the median particle radius $r_{1,2}$ as:

$$r_{1,2} = \left(\frac{1}{r_1} + \frac{1}{r_2}\right)^{-1} \quad \textbf{(A14)}$$

$$h_c = \frac{r_c^2}{r_{1,2}} \quad \textbf{(A15)}$$

Thus, Eqn. (A13) is now expressed as:

$$F_{H0} + F_N = \pi \; r_{1,2} \; p_f \left(\kappa_A - \kappa_p\right) h_c \qquad \textbf{(A16)}$$

If two particles with the same diameter d are considered, Eqn. (4) is obtained from Eqn. (A16).

In order to obtain the adhesion force model proposed by Tomas, that is the negative force necessary to separate the particles in point A and reported in Eqns. (9)-(10) the following approach can be considered. According to models developed by Krupp (1967) and Dahneke (1972) the expression of adhesion forces is the sum of adhesion forces F_{H0} plus an attractive/repulsive force contribution due to the van der Waals force contribution across the plastically deformed contact area A_c:

$$F_H = F_{H0} + A_c \; p_{VdW} = F_{H0} + p_f \; \kappa_p \; \pi \; r_{1,2} \; h_c \qquad \textbf{(A17)}$$

Using Eqn.(A16) it is:

$$\pi \; r_{1,2} \; p_f \; h_c = (F_{H0} + F_N)/\left(\kappa_A - \kappa_p\right) \qquad \textbf{(A18)}$$

In Eqn. (A17)

$$F_H = F_{H0} + \frac{\kappa_p}{\left(\kappa_A - \kappa_p\right)}(F_{H0} + F_N) \qquad \textbf{(A19)}$$

Therefore, considering Eqn. (10), the coefficient κ_A is expressed as:

$$\kappa_A = \kappa_p \frac{1 + \kappa}{\kappa} \qquad \textbf{(A20)}$$

And so:

$$F_H + F_N = \pi \; r_{1,2} \; p_f \; \kappa_A \; h_c \; \kappa_p \frac{1 + \kappa}{\kappa} = (F_H - F_{H0}) \frac{1 + \kappa}{\kappa} \qquad \textbf{(A21)}$$

And finally Eqn. (9) is obtained:

$$F_H = F_{H0} \; (1 + \kappa) + \kappa \; F_N \qquad \textbf{(A22)}$$

9. Nomenclature

C	cohesion (Pa)
A_c	total contact deformation area (m^2)
A_{el}	elastic particle deformation area (m^2)
A_{pl}	plastic particle deformation area (m^2)
$C_{H,sfs}$	Hamaker solid-fluid-solid constant (J)
d	particle diameter (m)
d_{16}	16^{th} percentile size (m)
d_{50}	50^{th} percentile size (m)
d_{84}	84^{th} percentile size (m)
d_{sv}	Sauter mean diameter (m)
E	Young modulus (N m^{-2})
E*	Hertz modulus of elasticity (N m^{-2})
f_c	unconfined yield strength (Pa)
ff_c	flow factor (-)
F_0	adhesion force without any consolidation (N)
F_C	contact force between particles (N)
F_H	adhesion force (N)
F_{H0}	adhesion force without any consolidation and contact flattening (N)
F_N	compressive normal force (N)
h_c	height of flattening (m)
$h_{c,f}$	height of flattening for incipient yielding at $p = p_f$ (m)
HDFs	Hydrodynamic forces
H_V	Vickers Hardness (Pa)
IPFs	Interparticle forces
NR	natural rutile sample
p_f	compressive yield strength (Pa)
p_{VdW}	attractive van der Waals pressure (Pa)
P	Pressure (Pa)
PSD	particle size distribution
RDS	relative diameter spread (-)
r_c	contact radius (m)
r_{el}	mean curvature radius for elastic contact point (m)
r_p	mean curvature radius for plastic contact point (m)
SR	synthetic rutile sample
SYL	stationary yield locus
T	temperature (°C)
TS	titania slag sample
YL	yield locus
z_0	characteristic molecular separation distance (m)
α	ratio between p_f at high temperature and p_f at ambient temperature
ε	bed voidage (-)
ε_0	fixed bed voidage (-)
κ	elastic-plastic consolidation coefficient (-)
κ_A	elastic-plastic contact area coefficient (-)
κ_p	plastic repulsion coefficient for Tomas model (-)
κ_{pl}	plastic repulsion coefficient for Rumpf-Molerus model (-)
ν	Poisson ratio (-)
ρ_b	powder bulk density (kg m^{-3})
ρ_p	particle density (kg m^{-3})

σ	normal stress (Pa)
σ_0	isostatic tensile strength of unconsolidated powder (Pa)
σ_1	major principal stress (Pa)
σ_2	minor principal stress (Pa)
$\sigma_{M,st}$	centre of the Mohr circle for the steady-state flow (Pa)
σ_{pre}	normal pre-shear stress (Pa)
$\sigma_{R,st}$	radius of the Mohr circle for the steady-state flow (Pa)
σ_t	tensile strength (Pa)
τ	shear stress (Pa)
τ_{pre}	tangential pre-shear stress (Pa)
ϕ_i	angle of internal friction (deg.)
ϕ_{st}	steady-state angle of internal friction (deg.)

10. References

Ashton, M.D., Cheng, D.C.H., Farley, R., Valentin, F.H.H., 1965. Some investigations into the strength and flow properties of powders. Rheol. Acta 4, 206–218. doi:10.1007/BF01969257

Barletta, D., Poletto, M., 2012. Aggregation phenomena in fluidization of cohesive powders assisted by mechanical vibrations. Powder Technol. 225, 93–100. doi:10.1016/j.powtec.2012.03.038

Bennett, J.M., Pelletier, E., Albrand, G., Borgogno, J.P., Lazarides, B., Carniglia, C.K., Schmell, R. a, Allen, T.H., Tuttle-Hart, T., Guenther, K.H., Saxer, a, 1989. Comparison of the properties of titanium dioxide films prepared by various techniques. Appl. Opt. 28, 3303–3317. doi:10.1364/AO.28.003303

Bruni, G., Barletta, D., Poletto, M., Lettieri, P., 2007a. A rheological model for the flowability of aerated fine powders. Chem. Eng. Sci. 62, 397–407. doi:10.1016/j.ces.2006.08.060

Bruni, G., Lettieri, P., Newton, D., Barletta, D., 2007b. An investigation of the effect of the interparticle forces on the fluidization behaviour of fine powders linked with rheological studies. Chem. Eng. Sci. 62, 387–396. doi:10.1016/j.ces.2006.08.059

Bruni, G., Lettieri, P., Newton, D., Yates, J.G., 2006. The influence of fines size distribution on the behaviour of gas fluidized beds at high temperature. Powder Technol. 163, 88–97. doi:10.1016/j.powtec.2006.01.007

Chen, P., Yuan, Z., Shen, X., Zhang, Y., 2012. Flow properties of three fuel powders. Particuology 10, 438–443. doi:10.1016/j.partic.2011.11.013

Cheng, D.C.-H., 1968. The tensile strength of powders. Chem. Eng. Sci. 23, 1405–1420. doi:10.1016/0009-2509(68)89051-7

Chirone, R., Barletta, D., Lettieri, P., Poletto, M., 2016. Bulk flow properties of sieved samples of a ceramic powder at ambient and high temperature. Powder Technol. 288, 379–387. doi:10.1016/j.powtec.2015.11.040

Dahneke, B., 1972. The influence of flattening on the adhesion of particles. J. Colloid Interface Sci. 40, 1–13. doi:10.1016/0021-9797(72)90168-3

Fitzpatrick, J., Barringer, S., Iqbal, T., 2004. Flow property measurement of food powders and sensitivity of Jenike's hopper design methodology to the measured values. J. Food Eng. 61, 399–405.

Formisani, B., Girimonte, R., Mancuso, L., 1998. Analysis of the fluidization process of particle beds at high temperature. Chem. Eng. Sci. 53, 951–961.

Formisani, B., Girimonte, R., Pataro, G., 2002. The influence of operating temperature on the dense phase properties of bubbling fluidized beds of solids. Powder Technol. 125, 28–38.

Forsyth, A.J., Hutton, S., Rhodes, M.J., 2002. Effect of cohesive interparticle force on the flow characteristics of granular material. Powder Technol. 126, 150–154. doi:10.1016/S0032-5910(02)00046-3

Frost, H.J., Ashby, M.F., 1982. Deformation-mechanism maps: The plasticity and creep of metals and ceramics. Oxford, Pergamon Press 175. doi:10.1016/0378-3804(84)90015-9

Fu, X., Huck, D., Makein, L., Armstrong, B., Willen, U., Freeman, T., 2012. Effect of

particle shape and size on flow properties of lactose powders. Particuology 10, 203–208. doi:10.1016/j.partic.2011.11.003

Geldart, D., 1987. Gas Fluidization Technology. Wiley.

Gröger, T., Tüzün, U., Heyes, D.M., 2003. Modelling and measuring of cohesion in wet granular materials. Powder Technol. 133, 203–215. doi:10.1016/S0032-5910(03)00093-7

Guermazi, M., Hofler, H.J., Hahn, H., Averback, R.S., 1991. Temperature Dependence of the Hardness of Nanocrystalline Titanium Dioxide. J. Am. Ceram. Soc. 74, 2672–2674. doi:10.1111/j.1151-2916.1991.tb06819.x

Hencky, H., 1923. Über einige statisch bestimmte Fälle des Gleichgewichts in plastischen Körpern. Z. Angew. Math. Mech 747, 241–251.

Hertz, H., 1881. Ueber die Berührung fester elastischer Körper. J. für die reine und Angew. Math. 92, 156–171.

Hou, Q.F., Zhou, Z.Y., Yu, a. B., 2012. Micromechanical modeling and analysis of different flow regimes in gas fluidization. Chem. Eng. Sci. 84, 449–468. doi:10.1016/j.ces.2012.08.051

Hurley, J.P., Mukherjee, B., Mann, M.D., 2006. Assessment of filter dust characteristics that cause filter failure during hot-gas filtration. Energy and Fuels 20, 1629–1638. doi:10.1021/ef050303k

Ishlinsky, A.J., 1944. The axial-symmetrical problem in plasticity and the Brinell test. Theor. Res. Transl. 2, 47.

Janssen, H.A., 1895. Versuche uber Getreidedruck in Silozellen. Zeitschrift des Vereines Dtsch. Ingenieure 39, 1045–1049.

Jenike, A.W., 1962. Gravity flow of solids. Trans Instn Chem Engrs 40, 264.

Jenike, A.W., 1964. Storage and Flow of Solids, Bulletin No. 123. Bull. Univ. Utah 53.

Jenike, A.W., Elsey, P.J., Wooley, R.H., 1960. Flow properties of bulk solids. Proc Am. Soc Test. Mater. 60, 1168.

Johanson, K., Barletta, D., 2004. The influence of air counter-flow through powder materials as a means of reducing cohesive flow problems. Part. Part. Syst. Charact. 21, 316–325. doi:10.1002/ppsc.200400939

Kanaoka, C., Hata, M., Makino, H., 2001. Measurement of adhesive force of coal flyash particles at high temperatures and different gas compositions. Powder Technol. 118, 107–112. doi:10.1016/S0032-5910(01)00300-X

Kirby, R.K., 1967. Thermal Expansion of Rutile from 100 to 700 ° K. J. Res. Natl. Bur. Stand. (1934). 71A, 363–369. doi:10.6028/jres.071A.041

Kono, H., Aksoy, E., Itani, Y., 1994. Measurement and application of the rheological parameters of aerated fine powders—a novel characterization approach to powder flow properties. Powder Technol. 81, 177–187.

Krupp, H., 1967. Particle adhesion theory and experiment. Adv. Colloid Interface Sci. 1, 111–239. doi:10.1016/0001-8686(67)80004-6

Landi, G., Barletta, D., Poletto, M., 2011. Modelling and experiments on the effect of air humidity on the flow properties of glass powders. Powder Technol. 207, 437–443. doi:10.1016/j.powtec.2010.11.033

Lettieri, P., Macrì, D., 2016. Effect of Process Conditions on Fluidization. KONA Powder Part. J. 1–24. doi:10.14356/kona.2016017

Lettieri, P., Newton, D., Yates, J.G., 2002. Homogeneous bed expansion of FCC catalysts, influence of temperature on the parameters of the Richardson–Zaki equation. Powder Technol. 123, 221–231. doi:10.1016/S0032-5910(01)00463-6

Lettieri, P., Yates, J.G., Newton, D., 2000. The influence of interparticle forces on the fluidization behaviour of some industrial materials at high temperature. Powder Technol. 110, 117–127. doi:10.1016/S0032-5910(99)00274-0

Liang, C., Xie, X., Xu, P., Chen, X., Zhao, C., Wu, X., 2012. Investigation of influence of coal properties on dense-phase pneumatic conveying at high pressure. Particuology 10, 310–316. doi:10.1016/j.partic.2012.01.003

Medhe, M., Pitchumani, B., Tomas, J., 2005. Flow characterization of fine powders using material characteristic parameters. Adv. Powder Technol. 16, 123–135.

Molerus, O., 1975. Theory of yield of cohesive powders. Powder Technol. 12, 259–275.

Molerus, O., 1978. Effect of interparticle cohesive forces on the flow behaviour of powders. Powder Technol. 20, 161–175.

Molerus, O., 1982. Interpretation of Geldart's type A, B, C and D powders by taking into account interparticle cohesion forces. Powder Technol. 33, 81–87.

Molerus, O., 1994. Principles of Flow in Disperse Systems Von. Vak. Forsch. und Prax. 6, 233. doi:10.1002/vipr.19940060330

Mutsers, S.M.P., Rietema, K., 1977. The effect of interparticle forces on the expansion of a homogeneous gas-fluidized bed. Powder Technol. 18, 239–248. doi:10.1016/0032-5910(77)80014-4

Nedderman, R.M., 1992. Statics and Kinematics of Granular Materials. Cambridge University Press.

Pagliai, P., Simons, S.J.R., Rhodes, D., 2006. A novel experimental study of temperature enhanced cohesive interparticle forces. Powder Technol. 174, 71–74. doi:10.1016/j.powtec.2006.10.025

Pierrat, P., Agrawal, D.K., Caram, H.S., 1998. Effect of moisture on the yield locus of granular materials: Theory of shift. Powder Technol. 99, 220–227. doi:10.1016/S0032-5910(98)00111-9

Pierrat, P., Caram, H.S., 1997. Tensile strength of wet granula materials. Powder Technol. 91, 83–93. doi:10.1016/S0032-5910(96)03179-8

Pilpel, N., Britten, J.R., 1979. Effects of temperature on the flow and tensile strengths of powders. Powder Technol. 22, 33–44. doi:10.1016/0032-5910(79)85005-6

Poirier, J.P., 1985. Creep of crystals: high-temperature deformation processes in metals, ceramics and minerals. Cambridge University Press.

Quintanilla, M.A.S., Castellanos, A., Valverde, J.M., 2001. Correlation between bulk stresses and interparticle contact forces in fine powders. Phys. Rev. E. Stat. Nonlin. Soft Matter Phys. 64, 031301. doi:10.1103/PhysRevE.64.031301

Rietema, K., Cottaar, E., Piepers, H., 1993. The effects of interparticle forces on the stability of gas-fluidized beds—II. Theoretical derivation of bed elasticity on the basis of van der Waals forces between. Chem. Eng. Sci. 48, 1687–1697.

Ripp, M., Ripperger, S., 2010. Influence of temperature on the flow properties of bulk solids.

Chem. Eng. Sci. 65, 4007–4013. doi:10.1016/j.ces.2010.03.046

Ritala, M., Leskelä, M., Niinistö, L., Prohaska, T., Friedbacher, G., Grasserbauer, M., 1994. Surface roughness reduction in atomic layer epitaxy growth of titanium dioxide thin films. Thin Solid Films 249, 155–162. doi:10.1016/0040-6090(94)90754-4

Rumpf, H., 1970. Zur theorie der zugfestigkeit von agglomeraten bei kraftuebertragung an kontaktpunkten. Chemie Ing. Tech. 42, 538–540.

Schubert, H., Sommer, K., Rumpf, H., 1976. Plastische Verformung des Kontaktbereiches bei der Partikelhaftung. Chemie Ing. Tech. 48, 716–716. doi:10.1002/cite.330480816

Schulze, D., 1994a. A new ring shear tester for flowability and time consolidation measurements, in: Proc. 1st International Particle Technology Forum.

Schulze, D., 1994b. Development and application of a novel ring shear tester - Entwicklung und Anwendung eines neuartigen Ringschergerätes. Aufbereitungs-Technik 35, 524–535.

Schulze, D., 2007. Powders and bulk solids: behavior, characterization, storage and flow. Berlin.

Schwedes, J.J., 2003. Review on testers for measuring flow properties of bulk solids. Granul. Matter 5, 1–43. doi:10.1007/s10035-002-0124-4

Soediono, B., 2009. Elasticity, in: Mechanical Properties of Ceramics, Second Edition. John Wiley & Sons, Inc., Hoboken, NJ, USA, pp. 35–54. doi:10.1002/9780470451519.ch3

Stainforth, P.T., Ashley, R.C., 1973. An analytical hopper design method for cohesive powders. Powder Technol. 7, 215–243. doi:10.1016/0032-5910(73)80027-0

Stainforth, P.T., Ashley, R.C., Morley, J.N.B., 1971. Computer analysis of powder flow characteristics. Powder Technol. 4, 250–256. doi:10.1016/0032-5910(71)80045-1

Stainforth, P.T., Berry, R.E.R., 1973. A General Flowability Index for Powders. Powder Technol. 8, 243–251. doi:10.1016/0032-5910(73)80089-0

Tanaka, M., Komagata, M., Tsukada, M., Kamiya, H., 2008. Evaluation of the particle–particle interactions in a toner by colloid probe AFM. Powder Technol. 183, 273–281. doi:10.1016/j.powtec.2007.07.039

Teunou, E., Fitzpatrick, J.J., 1999. Effect of relative humidity and temperature on food powder flowability. J. Food Eng. 42, 109–116. doi:10.1016/S0260-8774(99)00087-4

Thornton, C., Ning, Z., 1998. A theoretical model for the stick/bounce behaviour of adhesive, elastic- plastic spheres. Powder Technol. 99, 154–162. doi:10.1016/S0032-5910(98)00099-0

Tomas, J., 2000. Particle Adhesion Fundamentals and Bulk Powder Consolidation. Kona 18, 157–169.

Tomas, J., 2001a. Assessment of Mechanical Properties of Cohesive Particulate Solids. Part 2: Powder Flow Criteria. Part. Sci. Technol. 19, 111–129. doi:10.1080/02726350152772065

Tomas, J., 2001b. Assessment of Mechanical Properties of Cohesive Particulate Solids. Part 1: Particle Contact Constitutive Model. Part. Sci. Technol. 19, 95–110. doi:10.1080/02726350152772056

Tomas, J., 2003. Mechanics of nanoparticle adhesion — A continuum approach. Part. Surfaces 8 Detect. Adhes. Removal, 1–47.

Tomas, J., 2004. Fundamentals of cohesive powder consolidation and flow. Granul. Matter 6, 75–86. doi:10.1007/s10035-004-0167-9

Tomasetta, I., Barletta, D., Lettieri, P., Poletto, M., 2012. The measurement of powder flow properties with a mechanically stirred aerated bed. Chem. Eng. Sci. 69, 373–381. doi:10.1016/j.ces.2011.10.056

Tomasetta, I., Barletta, D., Poletto, M., 2011. The Effect of Temperature on Flow Properties of Fine Powders. Chem. Eng. Trans. 24, 655–660.

Tomasetta, I., Barletta, D., Poletto, M., 2013. The High Temperature Annular Shear Cell: A modified ring shear tester to measure the flow properties of powders at high temperature. Adv. Powder Technol. 24, 609–617. doi:10.1016/j.apt.2012.11.007

Tomasetta, I., Barletta, D., Poletto, M., 2014. Correlation of powder flow properties to interparticle interactions at ambient and high temperatures. Particuology 12, 90–99. doi:10.1016/j.partic.2013.02.002

Wachtman, J.B., Tefft, W.E., Lam, D.G., Apstein, C.S., 1961. Exponential temperature dependence of Young's modulus for several oxides. Phys. Rev. 122, 1754–1759. doi:10.1103/PhysRev.122.1754

Walker, D.M., 1966. An approximate theory for pressures and arching in hoppers. Chem. Eng. Sci. 21, 975–997. doi:10.1016/0009-2509(66)85095-9

Walters, J.K., 1973. A theoretical analysis of stresses in axially-symmetric hoppers and bunkers. Chem. Eng. Sci. 28, 779–789. doi:10.1016/0009-2509(77)80012-2

Weidner, D., Wang, Y., Vaughan, M.T., 1994. Yield strength at high pressure and temperature. Geophys. Res. Lett.

Xie, H.Y., Geldart, D., 1995. Fluidization of FCC powders in the bubble-free regime: effect of types of gases and temperature. Powder Technol. 82, 269–277. doi:10.1016/0032-5910(94)02932-E

Zimmerlin, B., Leibold, H., Seifert, H., 2008. Evaluation of the temperature-dependent adhesion characteristics of fly ashes with a HT-rheometer. Powder Technol. 180, 17–20. doi:10.1016/j.powtec.2007.03.014